Computational and Structural Biotechnology Journal 31 (2026) 263–275

Contents lists available at ScienceDirect

Computational and Structural Biotechnology Journal

journal homepage: www.elsevier.com/locate/csbj

Research article

# Oxidative stress-driven transcriptomic remodeling in human astrocytes reveals network signatures associated with neurodegenerative and cardiovascular processes

Patricia M. Bota [a], Pol Picón-Pagès [b,c,d,e,f], Hugo Fanlo-Ucar [b], Saja Almabhouh [a], Oriol Bagudanch [b], Melisa E. Zeylan [g], Simge Senyuz [g], Patrick Gohl [a], Rubén Molina-Fernández [a], Narcis Fernandez-Fuentes [j], Eduard Barbu [k], Raul Vicente [k], Stanley Nattel [l,m,n], Angel Ois [o], Albert Puig-Pijoan [o], Jordi Garcia-Ojalvo [p], Ozlem Keskin [g,h], Attila Gursoy [g,i], Francisco J. Muñoz [b], Baldomero Oliva [a,*]

[a] Laboratory of Structural Bioinformatics (GRIB), Department of Medicine and Life Sciences, Universitat Pompeu Fabra, Barcelona, Spain
[b] Laboratory of Molecular Physiology, Department of Medicine and Life Sciences, Universitat Pompeu Fabra, Barcelona, Spain
[c] Molecular and Cellular Neurobiotechnology, Institute for Bioengineering of Catalonia (IBEC), Parc Científic de Barcelona, Baldiri and Reixac 15-21, Barcelona 08028, Spain
[d] Department of Cell Biology, Physiology and Immunology, Faculty of Biology, University of Barcelona, Barcelona, Spain
[e] Ciberned (Network Centre of Biomedical Research of Neurodegenerative Diseases), Institute of Health Carlos III, Madrid, Spain
[f] Institute of Neuroscience, University of Barcelona, Barcelona, Spain
[g] Computational Sciences and Engineering, Graduate School of Science and Engineering, Koç University, Istanbul, Türkiye
[h] Department of Chemical and Biological Engineering, Koç University, Istanbul, Türkiye
[i] Department of Computer Engineering, Koç University, Istanbul, Türkiye
[j] Institute of Biological, Environmental and Rural Science, Aberystwyth University, Aberystwyth SY23 3DA, United Kingdom
[k] Institute of Computer Science, University of Tartu, Estonia
[l] Department of Medicine and Research Center, Montreal Heart Institute and Université de Montréal, Montréal, Canada
[m] Institute of Pharmacology, West German Heart and Vascular Center, University Duisburg-Essen, Duisburg, Germany
[n] IHU LIRYC and Fondation Bordeaux Université, Bordeaux, France
[o] Department of Neurology, Hospital Del Mar. Hospital Del Mar - Medical Research Institute and Universitat Pompeu Fabra, Barcelona, Spain
[p] Laboratory of Dynamical Systems Biology, Department of Medicine and Life Sciences, Universitat Pompeu Fabra, Barcelona, Spain

ARTICLE INFO

*Keywords:*
Aging-associated proteomic remodeling
Oxidative stress-responsive astrocyte pathways
Network-based gene-disease prioritization
Structurally vulnerable proteinprotein interfaces
Neurodegeneration-cardiovascular disease crosstalk
Astrocytic vulnerability networks
Proteostasis and mitochondrial dysfunction
Structure-guided variant impact prediction
Telomere and nuclear envelope integrity

ABSTRACT

Astrocytes are central to brain homeostasis, supporting neuronal metabolism, synaptic activity, and the blood–brain barrier. With aging, these glial cells undergo molecular and functional changes that weaken support functions and promote neuroinflammation, contributing to neurodegeneration. Yet the systems-level mechanisms by which astrocytes respond to aging-related stressors remain poorly defined in human models. Because aging also heightens risk for cardiovascular disease, cognitive impairment, type 2 diabetes, and systemic inflammation, clarifying shared astrocytic pathways is critical for understanding brain–body crosstalk. Using an in vitro human astrocyte model exposed to sublethal oxidative stress (10 μM $H_2O_2$) as a proxy for age-related cellular stress, we profiled transcriptomic changes and identified differentially expressed genes across antioxidant defenses, proteostasis, transcriptional regulation, vesicular trafficking, and inflammatory signaling. We then performed network-prioritization analyses on a curated human protein–protein interactome: one seeded with the astrocyte oxidative stress responsive genes and six with phenotype-associated gene sets (Alzheimer's disease, cardiovascular disease, cognitive impairment, type 2 diabetes, oxidative stress, and inflammation). Intersecting the top 5 % scoring genes from each run yielded a 127-gene core shared across all seven, enriched for proteostasis, DNA repair, mitochondrial regulation, and telomere and nuclear envelope maintenance. Structure-guided analyses highlighted vulnerable interfaces, including lamin A/C–lamin B1, α-actinin–filamins, 14–3–3 dimers, and aminoacyl-tRNA synthetase assemblies, where pathogenic variants are predicted to destabilize or aberrantly stabilize protein interactions. Structure-based interface predictions also highlight potential interactions between

* Corresponding author.
*E-mail address:* baldo.oliva@upf.edu (B. Oliva).

https://doi.org/10.1016/j.csbj.2025.12.032
Received 14 November 2025; Received in revised form 29 December 2025; Accepted 30 December 2025
Available online 31 December 2025
2001-0370/© 2026 The Authors. Published by Elsevier B.V. on behalf of Research Network of Computational and Structural Biotechnology. This is an open access article under the CC BY-NC-ND license (http://creativecommons.org/licenses/by-nc-nd/4.0/).

Downloaded from https://spj.science.org at Koc Universitesi Suna Kirac on July 02, 2026

amyloid precursor protein (APP) and valosin-containing protein (VCP), and between p53 and 14–3-3ζ, potentially linking proteostasis and stress signaling. Together, these analyses identify a conserved astrocyte-centered network signature that may relate neurodegenerative and cardiovascular processes, and prioritize structurally testable candidates for biomarker and intervention hypothesis testing.

## 1. Introduction

Astrocytes, the most abundant glial cells in the brain, are essential for maintaining neuronal health and central nervous system (CNS) homeostasis [1]. They maintain extracellular ionic balance and neurotransmitter homeostasis [1,2], modulate synaptic activity through gliotransmitter release [3,4], provide metabolic support to neurons [5], and help regulate cerebral blood flow while reinforcing the blood–brain barrier (BBB) [6]. Astrocytes also react dynamically to neural injury or disease by entering reactive states and releasing signaling molecules [1]. In neurodegenerative conditions such as Alzheimer's disease (AD), astrocytes can become excessively reactive and produce reactive oxygen species (ROS) in response to amyloid-β (Aβ) [7]. These ROS exacerbate neuronal oxidative damage, fueling a self-perpetuating cycle of neuroinflammation that further impairs astrocytes and neurons [8,9]. Chronic oxidative stress in astrocytes disrupts neurotransmitter regulation and weakens BBB integrity, ultimately amplifying neurodegenerative processes [9]. Notably, astrocyte dysfunction is influenced by systemic vascular factors: cardiovascular pathology can trigger or amplify glial stress responses, placing astrocytes at the nexus of cardiovascular and neurodegenerative processes [10,11]. Cardiovascular disease (CVD) and cognitive impairment (CI) are closely interrelated in the aging population, sharing numerous risk factors and underlying molecular mechanisms [12–14]. CI encompasses conditions from mild cognitive deficits to severe dementia, with AD and vascular dementia being the most prevalent forms [15,16]. CVD can accelerate cognitive decline by chronically reducing cerebral perfusion and triggering neuronal dysfunction [17]. Thus, elucidating the molecular links between CVD and CI is vital for developing novel biomarkers, therapeutic interventions, and preventive strategies. Emerging evidence suggests that astrocytes exposed to chronic oxidative stress (OS) and inflammatory signals contribute to cognitive deterioration [18,19]. Moreover, systemic metabolic conditions such as coronary heart disease, atherosclerosis, and type 2 diabetes (T2D), which are strongly correlated with both CI and AD, can directly or indirectly impair astrocytic function [20,21]. This multifactorial convergence implies that astrocytes lie at the intersection of neurodegenerative and systemic aging-related processes, warranting a systems-level approach to decipher common mechanisms. Protein–protein interaction (PPI) networks provide a powerful framework to integrate diverse molecular data and identify hub proteins that link converging pathological pathways. In this study, we combined transcriptomic profiling with network-based analysis and structural modeling to investigate common mechanisms underlying astrocyte responses to oxidative stress in the context of aging-associated neurodegenerative and cardiovascular diseases. Using a human cortical astrocyte culture exposed to chronic sublethal oxidative stress (10 μM $H_2O_2$) to model a specific aspect of aging-related cellular stress [22], we first characterized global transcriptomic changes. We then ran seven separate network-prioritization analyses: one seeded with the astrocyte $H_2O_2$ response and six seeded with the gene sets for AD, CVD, CI, T2D, inflammation, and OS. In each run, genes were ranked by topological proximity to the seeds, and the top 5 % defined the phenotype subnetwork. Finally, we evaluated how disease-associated mutations might disrupt critical protein-protein interfaces. This integrative strategy, spanning from gene expression profiles to systems-level networks to atomic-level interactions, provides a comprehensive view of how astrocytic stress responses may bridge neurodegenerative and cardiovascular disease processes. Our findings reveal conserved molecular vulnerabilities in oxidatively stressed human astrocytes and offer mechanistic insights that could inform biomarkers and therapeutic targets for neurodegenerative and cardiovascular disorders associated with aging and oxidative stress.

## 2. Materials & methods

### 2.1. Cell line

Human cortical astrocytes (HA) were purchased from ScienCell. Cells were maintained in astrocyte medium (AM; ScienCell) supplemented with 2 % fetal bovine serum (FBS; HyClone), 1 % astrocyte growth supplement (ScienCell) and 1 % penicillin–streptomycin (Gibco). Cultures were maintained at 37°C in a humidified incubator with 5 % $CO_2$.

### 2.2. Cell viability assays

Cells were seeded into 96-well plates at a density of $2.5 \times 10^4$ cells per well. They were then treated with increasing concentrations of $H_2O_2$ (Merck) for 24 h. After treatment, 10 % of total well volume of 3-(4,5-dimethylthiazol-2-yl)-2,5-diphenyltetrazolium bromide (MTT) stock solution (Sigma) made with 5 mg/mL in Phosphate Buffered Saline (PBS) was added to each well and incubated for 2 h. MTT reduction was determined in a plate reader spectrophotometer at 540 and 650 nm. Control cell values were assumed as a 100 % of survival and cell viability was calculated as follows:

$$Cell\ viability(\%) = \frac{\left(A_{540}^{sample} - A_{650}^{sample}\right)}{\left(A_{540}^{control} - A_{650}^{control}\right)} \times 100$$

Where $A_{540}^{\text{sample}}$ is the absorbance of treated cells measured at 540 nm (MTT formazan signal); $A_{650}^{\text{sample}}$is the absorbance of treated cells measured at 650 nm (background/reference wavelength); $A_{540}^{\text{control}}$ is the absorbance of control (untreated) cells measured at 540 nm, assumed to represent 100 % viability; and $A_{650}^{\text{control}}$ is the absorbance of control (untreated) cells measured at 650 nm

### 2.3. Transcriptomic analysis

Cells were seeded in 6-well plates at a density of 5 × 10^5 cells/well and left to grow for two days. After washing twice with PBS and once with FBS-free AM medium, cells were treated with 10 μM $H_2O_2$ in 1 mL of FBS-free AM medium for 24 h. Treatments were performed in three independent experiments (n = 3).

Total RNA was extracted, and its quality and concentration were assessed using an Agilent TapeStation 4200 with RNA ScreenTape. Polyadenylated RNA was captured from 100 ng of total RNA using the NEBNext Poly(A) mRNA Magnetic Isolation Module (New England BioLabs, Ipswich, MA). Stranded RNA-seq libraries were prepared using the NEBNext Ultra II Directional RNA Library Prep Kit for Illumina (New England BioLabs) according to the manufacturer's instructions. The libraries were amplified by PCR using NEBNext Multiplex Oligos for Illumina (Dual Index Primers Set 1; New England BioLabs). Library quality and size distribution were verified on an Agilent TapeStation 4200 with High Sensitivity D1000 ScreenTape. Finally, libraries were pooled and sequenced (2 ×75 bp paired-end) on an Illumina NextSeq 500 High Output flow cell. Reads were aligned with STAR v2.5.2b to GRCh38 (annotation Ensembl v109), and gene-level counts were generated with HTSeq and differential expression was performed using

Downloaded from https://spj.science.org at Koc Universitesi Suna Kirac on July 02, 2026

limma-voom.

The results from the transcriptomic analysis including the statistical analysis are included in Supplementary Table 1 (overexpressed genes) and Supplementary Table 2 (repressed genes). The statistical analysis includes: Base Mean, Base Variance, All Zero, Dispersion Gene Estimate (Disp. Gene Est.), Dispersion Gene Iterative Estimate (Disp. Gene Iter.), Dispersion Fit (Disp. Fit), Dispersion, Dispersion Iterative Estimate (Disp. Iter.), Dispersion Outlier (Disp. Outlier), Dispersion Maximum A Posteriori (Disp. MAP), Log Fold Change, Average Expression (Aver. Expres.), Student's t-statistic, P-Value, Adjusted P-Value (Adj. P-Val) and B-statistic (B). Genes were selected based on a statistical criterion of an adjusted P-value less than 0.1, without fold-change cut-off (a full report is accessible in the Supplementary File 1).

### 2.4. Protein–protein interaction network assembly

We built the network of protein–protein interactions (PPI) using BIANA [23], a Python framework for integrating biological data. First, we retrieved the most recent interaction datasets from IntAct [24], BioGRID [25], HIPPIE [26] and InnateDB [27], and supplemented them with annotations from UniProt [28], Reactome [29], NCBI Gene [30], Taxonomy, PSI-MI-OBO, GO [31,32], HGNC [33], ConsensusPathDB [34], I2D [35] and DisGeNET [36].

Following BIANA's guidelines, we parsed each dataset without altering its original identifiers or metadata. After loading all sources into BIANA's knowledge database, we unified equivalent entries across resources: proteins sharing a common Entrez Gene ID or, when that was unavailable, both the same Taxonomy ID and identical amino-acid sequence, were merged into single entities. Each consolidated record was then assigned a unique BIANA identifier, effectively reducing redundancy while preserving full traceability.

The human-specific protein interaction network (PIN) was retrieved from the unified BIANA database. To reduce biases typically associated with detection methods favoring well studied proteins, we applied stringent filtering criteria, selecting only high confidence interactions validated by relatively unbiased experimental techniques. Specifically, accepted interaction methods included cross-linking studies, classical two-hybrid, two-hybrid arrays, two-hybrid prey pooling validated two-hybrid, two-hybrid pooling, biochemical assays, proximity labeling technology, and enzymatic studies. After filtering, the human protein–protein interaction network used for downstream analyses comprised 15,990 proteins connected by 690,161 undirected interactions and served as input for gene prioritization with the GUILD [37] framework. Relative to the pre-filter BIANA network (28,680 proteins and 16,986,854 interaction records), this corresponds to the retention of 55.8 % of proteins and 4.06 % of interaction records following restriction to selected "less biased" experimental methods, reflecting stringent confidence-based filtering. Despite this substantial reduction in network density, the final network remained highly connected, with an average node degree of 86.32, a global clustering coefficient (transitivity) of 0.466, a mean local clustering coefficient of 0.189, and 99.98 % of nodes contained within the largest connected component.

### 2.5. Selection of genes associated with pathophenotypes

Genes linked to specific phenotypes were selected from databases using keyword searches and association data. DisGeNET and OMIM [38] were employed to retrieve genes associated with AD, T2D, and CI, while gene descriptions in UniProt were used to identify those related to OS and inflammation. For CVD, we used keyword combinations across DisGeNET and UniProt to gather relevant gene associations. This approach ensured comprehensive coverage of genes linked to the targeted aging-associated conditions. In addition, we selected a set of phenotypes expected to be unrelated to ageing or to the pathophenotypes investigated in this study, which were used as negative controls to validate our approach. These included albinism, pachyonychia, achondroplasia, congenital myasthenic syndrome, primary ciliary dyskinesia, and cleft palate.

### 2.6. Prioritization of genes/proteins

We prioritized genes by propagating relevance scores from known disease-associated "seed" genes across the PPI network and integrating the outputs of multiple complementary algorithms into a single consensus ranking. For this purpose, we used GUILD [37], a genome-wide network-based disease-gene prioritization framework that identifies candidate genes based on their topological proximity to seeds in the interactome. GUILD implements three topology-based algorithms: NetShort, which ranks genes by their weighted shortest-path distances to seed nodes, emphasizing proteins that lie on minimal connection routes; NetZcore, which propagates relevance through immediate neighbors and applies z-score normalization against randomized networks to reduce hub bias; and NetScore, which iteratively diffuses scores along shortest paths from seeds, updating rankings over multiple rounds until convergence. In addition to these local topology-based algorithms, GUILD includes four global diffusion and propagation methods that disseminate relevance across the entire network: PageRank with priors [39], Functional Flow [40], Random Walk with Restart [41], and Network Propagation [42]. We also incorporated DIAMOnD [43], which extends disease-related modules by iteratively adding proteins based on statistically significant connectivity to existing seeds, calculated via hypergeometric testing. Individual scores from all seven methods were normalized and aggregated into a unified consensus score. For each phenotype-specific run, we obtained node scores from eight complementary methods implemented in GUILD (NetShort, NetZcore, NetScore, PageRank with priors/NetRank, Functional Flow, Random Walk with Restart/NetWalk, Network Propagation/NetProp) together with DIAMOnD. For every method, scores were linearly rescaled to the 0,1 interval, and the final consensus score for each node was defined as the mean of its normalized scores across the eight methods. Genes were then ranked by this consensus, and the top 5 % were retained as the phenotype subnetwork.

### 2.7. Functional enrichment

We assessed the overrepresentation of biological functions among both the seed proteins and the top-ranked candidate genes. Functional annotations were derived from Gene Ontology (GO) biological process terms and Reactome pathways. To ensure high-confidence results, only GO annotations supported by curated or experimental evidence codes (EXP, IDA, IMP, IGI, IEP, ISS, ISA, ISM, ISO) were included. Enrichment was evaluated using a one-sided Fisher's exact test, comparing the observed overlap between the gene sets and annotated terms against random expectation. The background set used for functional enrichment analyses consisted of the 15,990 proteins comprising the protein–protein interaction network. To account for multiple testing, p-values were corrected using both the Benjamini-Hochberg [44] false discovery rate procedure and the Bonferroni correction. Annotations with an FDR-adjusted p-value below 0.05 were considered significantly enriched.

### 2.8. Structure modeling of PPIs

Experimentally solved binary complexes currently cover less than 5 % of known human protein–protein interactions [45], making it necessary to rely on predicted structures for large-scale interactome analyses. To obtain three-dimensional models for the prioritized protein–protein interactions we used two sources: (1) the Comparative Modeling and Data-Driven Docking (CM2D3) [46] database and (2) the Protein Interactions by Structural Matching (PRISM) [47] web server. CM2D3 provides predicted complex models derived by both homology

Downloaded from https://spj.science.org at Koc Universitesi Suna Kirac on July 02, 2026

modeling and data-driven docking, whereas PRISM is a knowledge-based PPI prediction server that matches input protein structures to experimentally resolved interface templates. The structures retrieved from CM2D3 were first subjected to energy minimization using FoldX [48] (v2025.12.31) to correct rotamer and backbone distortions (using the *RepairPDB* command). After repair, the FoldX *AnalyseComplex* routine was applied to each wild-type model to calculate its baseline binding free energy and to delineate interface residues (defined as any residue whose Cα atom lies within 12 Å of the partner chain). Pathogenic missense variants were obtained from ClinVar [49] (accessed June 2025) and mapped onto UniProtKB canonical sequences to ensure consistent residue numbering. Variants located at the predicted interface (i.e. coinciding with the annotated interface residues) were selected for in silico mutagenesis. Using FoldX's *BuildModel*, each single-point mutation was introduced into the repaired complex structure, followed by a second AnalyseComplex run to obtain the mutant binding energy. The change in interface stability (ΔΔG_interface) was then computed as the difference between mutant and wild-type binding free energies. Mutations yielding ΔΔG_interface $> 1$ kcal/mol were classified as destabilizing, in accordance with published FoldX benchmarks. In parallel we used PRISM to search for pairs of target structures whose surface patches resemble the two complementary sides of experimentally resolved template interfaces; candidate complexes are then energy minimized and ranked by a global binding-energy score. PRISM predictions were used to identify structurally plausible interfaces for high-priority interactions that lacked CM2D3 models.

## 3. Results

### 3.1. Transcriptional response in astrocytes under oxidative stress

To define a subtoxic oxidative-stress (OS) condition for transcriptomics, we measured astrocyte viability across increasing $H_2O_2$ doses (Fig. 1) and selected 10 μM $H_2O_2$ (24 h) as a high-but-sublethal exposure. Differentially expressed genes are summarized in Supplementary Fig. 1 (upregulated) and Supplementary Fig. 2 (downregulated), with full statistics in Supplementary Tables 1 and 2.

Overall, mild OS elicited a biphasic transcriptional response: induction of redox/proteostasis/translation and trafficking components consistent with acute stress buffering, alongside repression of transcriptional regulation, signaling, transport/cytoskeletal organization, and genome maintenance. Changes that may support short-term survival while reducing homeostatic capacity if stress persists.

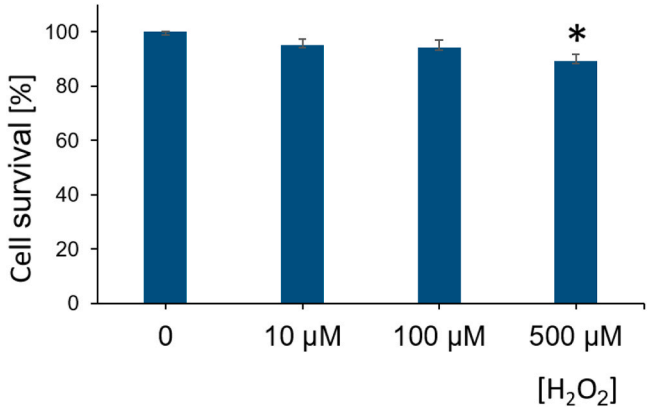



**Fig. 1.** Dose-dependent effect on the viability of human astrocytes in culture. The human astrocyte cell line (HA) was treated with increasing concentrations of $H_2O_2$ for 24 h. Cell survival was measured by MTT reduction and expressed as a percentage relative to the control assumed as 100 %. Data represent the mean ± SEM of 3 independent experiments performed in triplicate. * $p < 0.05$ vs. the control, as determined by ANOVA followed by Bonferroni post-hoc test.

Among upregulated genes (Supplementary Table 1), mitochondrial ROS handling and redox defense were prominent, including PRDX5 and ROMO1, consistent with reinforcement of peroxide detoxification and mitochondrial homeostasis under OS. [50,51] MIF also increased, linking stress responses with immune/inflammatory signaling. [52] Proteostasis support was strengthened through increased expression of STUB1 (CHIP) and RNA/protein-handling factors (SERF2, NUDC, TRMT112), consistent with enhanced folding and quality control under stress. [53–56] In parallel, induction of translation-related genes (e.g., RPS9, RPL41, POLR3K, RRP7A) and the tRNA-modifying enzyme CTU1 suggests an effort to preserve proteome integrity and translational accuracy. [57] Several signaling and trafficking components were also induced (e.g., CYBA, GRK6, DVL1, RAB13, YIF1B), consistent with activation of redox-linked signaling and vesicle/membrane dynamics. [58–62] Finally, increased expression of cell-cycle/vascular-associated genes (e.g., PKMYT1, MXD4, EGFL7) suggests OS-associated remodeling programs that could influence glial state and neurovascular interactions. [63]

In contrast, downregulated genes (Supplementary Table 2) concentrated in functions required for adaptive regulation and long-term maintenance. Multiple transcription and chromatin regulators (e.g., KLF12, CHD9, ASXL2, JMJD1C, KDM3A, AFF4) decreased, and repression of TEAD1 suggested reduced growth/survival transcriptional output. [64] Genes supporting intracellular transport and structural organization were also reduced (VPS13A, VPS13C, ARFGEF1, DYNC2H1, RANBP2; DOCK9, PSD3), consistent with constrained trafficking and cytoskeletal remodeling capacity under OS. [65–68] Neurotrophic/cytokine signaling competence may also be weakened, as IL6ST and LIFR decreased, together with pathway components such as SOS1, TAOK1, and BMPR2. [69–71] Notably, several DNA damage response/repair genes (ATM, SETX, SMG1, CDK12, TLK1) were repressed. [72,73] Decreased expression of adhesion/ECM and BBB-relevant genes (ITGAV, VCAN, DST, HMCN1, CAMSAP2) and of the redox-support gene SLC7A11 points to vulnerabilities in barrier/structural support and glutathione-related antioxidant capacity. [74–78] Finally, reduced expression of select protein-turnover components (LTN1, UBXN7, USP34) suggests that some degradative quality-control arms may be constrained even as other proteostasis pathways are induced. [79–81]

Together, these data indicate that sublethal $H_2O_2$ drives astrocytes to upshift immediate defenses (redox buffering, proteostasis, translation control, trafficking/signaling) while downshifting regulatory and maintenance programs (chromatin/transcriptional flexibility, receptor/signaling responsiveness, transport/cytoskeleton, and DNA repair), a tradeoff consistent with an acute adaptation that could become detrimental under prolonged OS.

### 3.2. Analysis of networks associated with selected phenotypes

To place the astrocyte transcriptomic changes in disease context, we mapped the $H_2O_2$-responsive genes onto a human protein–protein interaction (PPI) network. Each differentially expressed gene served as a seed, and we propagated influence across the interactome with the GUILD framework to identify proteins tightly connected to the astrocyte response. We then repeated this propagation for specific disease phenotypes (AD, CVD, T2D, CI, inflammation, OS) using their associated genes as additional seeds. Consensus across multiple topology-based algorithms yielded, for each phenotype, a prioritized subnetwork enriched for nodes central to disease biology and potentially influenced by astrocyte signals. This systems-level analysis highlights shared molecular players and pathways through which astrocyte oxidative stress may couple to neurodegenerative and cardiometabolic pathology.

Downloaded from https://spj.science.org at Koc Universitesi Suna Kirac on July 02, 2026

### 3.3. 2a. Network of proteins affected by oxidative stress in astrocytes (PAOSA)

We constructed two PAOSA subnetworks from the astrocyte differential-expression data: an astrocyte-overexpressed (AO) subnetwork seeded with genes significantly upregulated by $H_2O_2$ and an astrocyte-underexpressed (AU) subnetwork seeded with significantly downregulated genes. For each seed set, GUILD was run on the human PPI network, nodes were ranked by consensus score, and the top 5 % were retained as the corresponding PAOSA subnetwork. Using these top-ranked nodes, we observed coherent but opposing cellular programs. The AO subnetwork was enriched for protein homeostasis and translation (GO: cytoplasmic translation, translational initiation), proteostasis safeguards (chaperone-mediated protein folding, protein stabilization), ubiquitin-dependent quality control (regulation of protein ubiquitination), and RNA processing (mRNA splicing), with additional signals indicating feedback restraint of stress pathways (negative regulation of stress-activated MAPK cascade) and a telomere-maintenance module. In contrast, the AU subnetwork showed broad repression of gene-regulatory capacity, with strong enrichments for RNAPII-mediated transcriptional regulation (both positive and negative), chromatin remodeling and nucleosome disassembly, and regulation of miRNA transcription. The full list of prioritized genes and enriched pathways is provided in GitHub (see Data & Code Availability). Together, these network-level enrichments substantiate a dual response to mild $H_2O_2$ in astrocytes: activation of proteostatic and translational control programs alongside a coordinated inhibition of transcriptional/epigenetic machinery, supporting the protective-versus-vulnerable balance described above.

### 3.4. 2b. Networks of proteins for aging-associated pathophenotypes

The AD subnetwork recovers the canonical seeds (APP, MAPT, PSEN1, PSEN2, APOE, BACE1, CLU) and established risk/pathway genes (PICALM, BIN1, SORL1, CR1, CD33, IDE, IGF1R, INSR, BDNF, GSK3B), confirming disease specificity. The functional enrichment analysis supports amyloid-β biology [82] (cellular response to Aβ; negative regulation of Aβ formation; amyloid fibril/fiber formation), ER proteostasis [83] (positive regulation of ERAD; calnexin/calreticulin cycle; HSF1 activation) and mitochondrial protein quality control (UPRmt; mitochondrial protein degradation) [84], nitric-oxide biosynthetic regulation [85], and insulin/IGF-driven signaling converging on PI3K–AKT and MAPK/ERK [86]. Functional enrichment using Reactome further reinforces IGF1R–SHC and insulin-receptor cascades; activated NTRK2/TrkB via FRS2 and FRS3 with PI3K, PLCG1, and RAS branches; FOXO-mediated transcription; and insertion of tail-anchored proteins into the ER, integrating metabolic, synaptic-signaling (including NMDA receptor–RAS), vascular-NO, and proteostasis dimensions of AD. Additional supported signals include endothelial programs (VEGFR2/Tie2 with PECAM1 interactions), AGE–RAGE signaling, and CDK5-linked neurodegenerative pathways. Selenoamino-acid metabolism is also enriched.

The T2D subnetwork is driven by hallmark metabolic regulators: INSR, IRS1, AKT2, PPARG, TCF7L2, GCK, SLC30A8, HNF4A, IGF2BP2, PPARGC1A, SREBF1, LEPR, together with the seeded nodes LMNA (lamin A/C; nuclear-envelope and chromatin organization shaping metabolic gene programs) and TP53 (stress-responsive checkpoint integrating redox, mitochondrial, and apoptotic control). GO terms highlight glucose homeostasis, cellular response to insulin, insulin receptor signaling, positive regulation of D-glucose import, regulation of insulin secretion, leptin-mediated signaling, OS responses, and regulation of extrinsic apoptotic signaling via death-receptor pathways. Reactome reinforces this axis with insulin-receptor and IRS activation, SHC/IGF1R events [87], FOXO-mediated transcription [88], transcriptional regulation of white adipocyte differentiation [89], leptin signaling, and endothelial mechanotransduction through PIEZO1/integrins.

The CVD subnetwork brings together circadian clock genes (CLOCK, PER1/2, CRY1/2, NPAS2) with vascular and metabolic regulators (NOS3, ACE, AGT, VCAM1, ICAM1, VWF, APOB, APOE, LPL, ADRB1) and signaling nodes (AKT1, PTEN, PIK3CA, BDNF, SORT1), supporting endothelial function, lipoprotein handling, and circadian control of cardiovascular physiology. Enrichment signals converge on circadian control tightly linked to endothelial biology: clock programs [90] couple to disturbed-flow sensing through PIEZO1–integrin pathways and to nitric-oxide production [91], shaping vascular tone. Lipoprotein–platelet crosstalk is prominent, with LDL-driven platelet sensitization and chylomicron assembly/remodeling pointing to altered lipoprotein handling in the vessel wall [92]. We also see a dampening of glucocorticoid-receptor signaling and engagement of the angiopoietin–Tie2 axis, consistent with shifts in endothelial quiescence versus activation [93]. In parallel, NF-κB/IL-1 inflammatory activity [94] and strong cell-cycle/DNA-damage/senescence signatures indicate endothelial stress and turnover.

The inflammation subnetwork is anchored by the seed FLNC (filamin-C; an actin crosslinker that transduces mechanical forces at adhesion sites and organizes cytoskeletal signaling), alongside canonical innate–adaptive mediators IL1B, TNF, IL10, TLR2, TRL3 and TRL4, NFKB1, RELA, NFKB2, MYD88, CASP1, PYCARD, TBK1, PPARG, VCAM1, ICAM1, MMP2, MMP9, PARP1, HMGB1, and HSPA1A, HSPA1B, defining a strong inflammatory and stress-response core. Enrichment highlights canonical and non-canonical NF-κB activation; up-regulation of IL-1β/IL-6/IL-8 [95]; TLR signaling including TLR2: TLR6 and LPS responses; PI3K–AKT and ERK/JNK cascades; chemokine production; endothelial migration and vascular remodeling; antibacterial defense; regulation of superoxide and nitric oxide [96]; LUBAC-mediated linear polyubiquitination [97]; and modulation of extrinsic apoptotic signaling.

The CI subnetwork is dominated by peroxisome-biogenesis genes (multiple PEX family members) and neuronal/repair factors (APP, ATXN1, FLNA, UBA1), together with mitochondrial and DNA-repair modules (SDH subunits, ERCC2, ERCC3, ERCC4, ERCC5, XPA, XPC, ATR, APTX, XRCC4) and signaling nodes (INSR, AKT1, PIK3CA, PTEN). Enrichments focus on peroxisome organization and matrix import (receptor recycling, substrate release, docking, translocation, membrane import), nucleotide-excision repair and homologous recombination, cellular responses to reactive oxygen species, and pexophagy, supporting a CI network centered on peroxisome biogenesis/turnover [98] and DNA-damage repair [99].

The OS subnetwork recovers a core redox/stress architecture: NFE2L2, NRF2, SOD1, SOD2, CAT, PRDX1–6 (i.e. PRDX1, PRDX2, etc. up to PRDX6), TXNRD1, GSR, PARK7, G6PD, HMOX2, together with mitochondrial quality-control, DNA-repair, proteostasis, and survival regulators (TP53, MAPK14, AKT1, AKT2, FOXO1, HSPA1A, HSPA1B, HSPB1, PARP1, APEX1, RAD51, XRCC3, ERCC3, PRKN,PINK1, PRDX3, PRDX5). Enrichment profiles emphasize cellular and organismal responses to oxidative stress and hydrogen peroxide, suppression of ROS-induced intrinsic (neuronal) apoptosis, base-excision and transcription-coupled nucleotide-excision repair, DNA-damage responses [100], regulation of mitochondrial membrane potential and organization, induction of autophagy [101], negative regulation of ROS metabolism, protein repair, $H_2O_2$ and superoxide detoxification, negative TOR signaling, ubiquitination control, and PERK-mediated UPR.

Interestingly, a small set of non-seed genes consistently achieve high ranks. Most notably, TGOLN2 (TGN46) and the RPA protein complex, and in several networks LMNA, recur as prominent hubs. This behavior aligns with network-propagation theory: algorithms such as NetShort, NetScore, NetZcore, and diffusion methods prioritize nodes that lie on many short paths between seed genes and that connect multiple functional modules. Functionally, TGOLN2 occupies the trans-Golgi sorting/trafficking nexus influencing secretory and membrane-protein routing; the RPA complex anchors DNA replication/repair and replication-stress

Downloaded from https://spj.science.org at Koc Universitesi Suna Kirac on July 02, 2026

responses; and LMNA contributes to nuclear-envelope and chromatin integrity. Their high connectivity and central placement in the interactome therefore make them robust cross-phenotype bridges, explaining why they rank highly even without being seeded a priori.

### 3.5. 2c. Overlap between the PAOSA networks and the networks of selected phenotypes

Intersecting the top 5 % GUILD-prioritized genes from the AO with those from AD, CVD, T2D, OS, inflammation, and CI uncovered a large shared core. As shown in Fig. 2, 127 genes are shared by the seven networks, an unexpectedly large intersection that suggests a shared, centrally connected module across these aging-associated conditions. Consistency across methods was high as most shared genes were recovered by multiple GUILD algorithms (Fig. 3), underscoring prioritization robustness. External validation against GenAge [102] identified 28/127 aging-annotated genes (hypergeometric p-value $\approx 4.8 \times 10^{-22}$), supporting the biological relevance of this core. The complete ranked gene lists for each phenotype, including consensus scores, are available in the GitHub repository (see Data & Code Availability). Several non-seed hubs in this shared core are noteworthy both for their biological roles and because they are structurally interrogated later in the study. ACTN4, together with FLNB and FLNC, exemplifies the prominence of cytoskeletal cross-linkers that integrate adhesion, force transmission, and signaling. LMNB1, which pairs with lamin A/C, anchors chromatin to the nuclear periphery, reinforcing the nuclear-envelope theme that recurs across phenotypes. Similarly, the RPA1–3 complex exemplifies replication-stress adaptation, while EEF1D and the aminoacyl-tRNA synthetases QARS1 and EPRS1 link translation elongation and multi-synthetase complex function to proteostasis and stress regulation. TPR, a nuclear-pore basket scaffold, and UBE2I/UBC9, the central SUMO E2 conjugase, extend this nuclear quality-control axis by coupling transport and genome-stability checkpoints to SUMOylation. Proteostasis control is also underscored by VCP (p97/TERA), an AAA+ ATPase directing ER-associated degradation and organelle quality control. In addition, a recurrent signaling dimension is provided by the 14–3–3 adaptor family: YWHAB, YWHAG, and YWHAZ join their seeded counterparts in scaffolding phospho-proteins to regulate apoptosis, stress adaptation, and metabolic responses. Finally, VIM stands out as a type-III intermediate filament that interfaces with 14–3–3 proteins and organizes stress-adaptive cytoskeletal remodeling. To define a cross-phenotype functional core, we intersected the Reactome enrichment results from the top 5 % GUILD-prioritized genes in each network. For every phenotype-specific subnetwork (AD, CVD, T2D, CI, inflammation, OS, AO), we retained Reactome pathways with FDR-adjusted $P < 0.05$ and then selected the terms that were significantly enriched in all seven. These shared pathways (Table 1) converge on stress-adaptation and proteostasis modules, including HSF1 activation and regulation of the heat-shock response, the calnexin/calreticulin ER-folding cycle, cytosolic tRNA aminoacylation, and initiation of nuclear-envelope reformation. We also observed signals across RAS-axis pathways (RAS-GTPase and RAS-GAP mutants; activation of RAS in immune cells), selenium-dependent amino-acid metabolism, and SARS-CoV-1/2 targeted host pathways, which often capture chaperone/ER-stress and MAPK components. Applying the same intersection strategy to GO Biological Process terms yielded a single annotation common to all seven subnetworks, 'positive regulation of telomere maintenance via telomerase', aligning with the nuclear-envelope/genome-stability theme. Repeating the overlap analysis with AU seeds yielded a highly consistent result: 107 genes were shared with the phenotype networks, of which [105] overlapped with the 127-gene core defined from the AO analysis. This near-identity indicates that both directions of expression change converge on the same molecular backbone. The few upregulated specific genes (e.g., IARS1, LARS1, QARS1, BAG6, GANAB, PDHA1, NDUFS3, PICALM, PRMT1, TXN, TOP1) reinforced themes of translation, proteostasis, and ER folding, whereas the two downregulated specific genes (ARF6, KRT31) mapped to peripheral immune and apoptosis pathways. Taken together, the underexpressed analysis functions mainly as a robustness check, while the 127-gene set serves as the principal core signature. The convergence of these results is consistent with a shared network architecture in which proteostasis and genome-maintenance modules are repeatedly prioritized across phenotypes, while also highlighting candidate nodes in signaling and metabolism. To assess the specificity of the shared molecular signature observed among ageing-associated phenotypes, we performed a negative control analysis using a set of diseases not primarily driven by ageing-related mechanisms (see the selected phenotypes in methods section). Applying the same network-based prioritization strategy to these unrelated conditions in combination with the astrocyte oxidative-stress network resulted in a markedly reduced and qualitatively distinct overlap. The intersection of the top 5 % GUILD-ranked genes across these networks comprised only 79 genes, substantially fewer than the 127-gene core identified for ageing-associated phenotypes. Moreover, pathway-level convergence was largely absent: Reactome analysis revealed only a single shared pathway, related to viral manipulation of host intracellular signaling, in stark contrast to the broad and coherent set of stress-response, proteostasis, metabolic, and signaling pathways consistently shared across the ageing-related conditions. The failure to recapitulate either the size or functional coherence of the ageing-associated core in this negative control shows that the extensive overlap observed among AD, CVD, T2D, CI, inflammation, and oxidative stress is not a trivial consequence of network topology or methodological bias. Instead, it reflects a biologically meaningful convergence of astrocyte-centered molecular programs that are specifically linked to ageing and age-associated disease processes (see details in Data and Code availability section).

## 4. Structural analysis of interactions

We next explored the potential structural impacts of the set of common prioritized network interactions, especially in the context of known disease-associated mutations. Some of these proteins have previously been associated with individual pathologies among those studied, but most had not, and none had been linked to all of them. For the interaction edges connecting the top 5 % of prioritized genes, we queried CM2D3 for structural models of those protein pairs and retrieved ~200 curated complexes, built by template-based modeling when homologs were available and by data-driven docking for novel pairs. It should be noted that these are computational models, and their reliability depends on the confidence of the underlying modeling. In the case of docking, this confidence is generally lower than that of poses derived from experimentally determined structures of homologous proteins. We then mapped ClinVar pathogenic/likely pathogenic missense variants onto predicted binding interfaces and used FoldX to estimate the change in binding free energy ($\Delta\Delta G$ = mutant − wild-type). By convention, positive $\Delta\Delta G$ indicates a destabilizing mutation (weaker binding), whereas negative $\Delta\Delta G$ indicates a stabilizing mutation (stronger or hyperstable binding). This variant-centric, structure-informed approach complements network level prioritization and mirrors emerging frameworks that map disease variants to modeled interactomes to generate mechanistic hypotheses (Fig. 4). Given the uncertainties inherent to predicted complexes and to FoldX energy functions, we interpret these $\Delta\Delta G$ estimates as qualitative, model-dependent indicators of the likely direction and relative magnitude of variant effects, rather than as precise quantitative measurements. Across CM2D3's template-based models, many disease variants were predicted to weaken protein–protein interactions (PPIs), compatible

Downloaded from https://spj.science.org at Koc Universitesi Suna Kirac on July 02, 2026

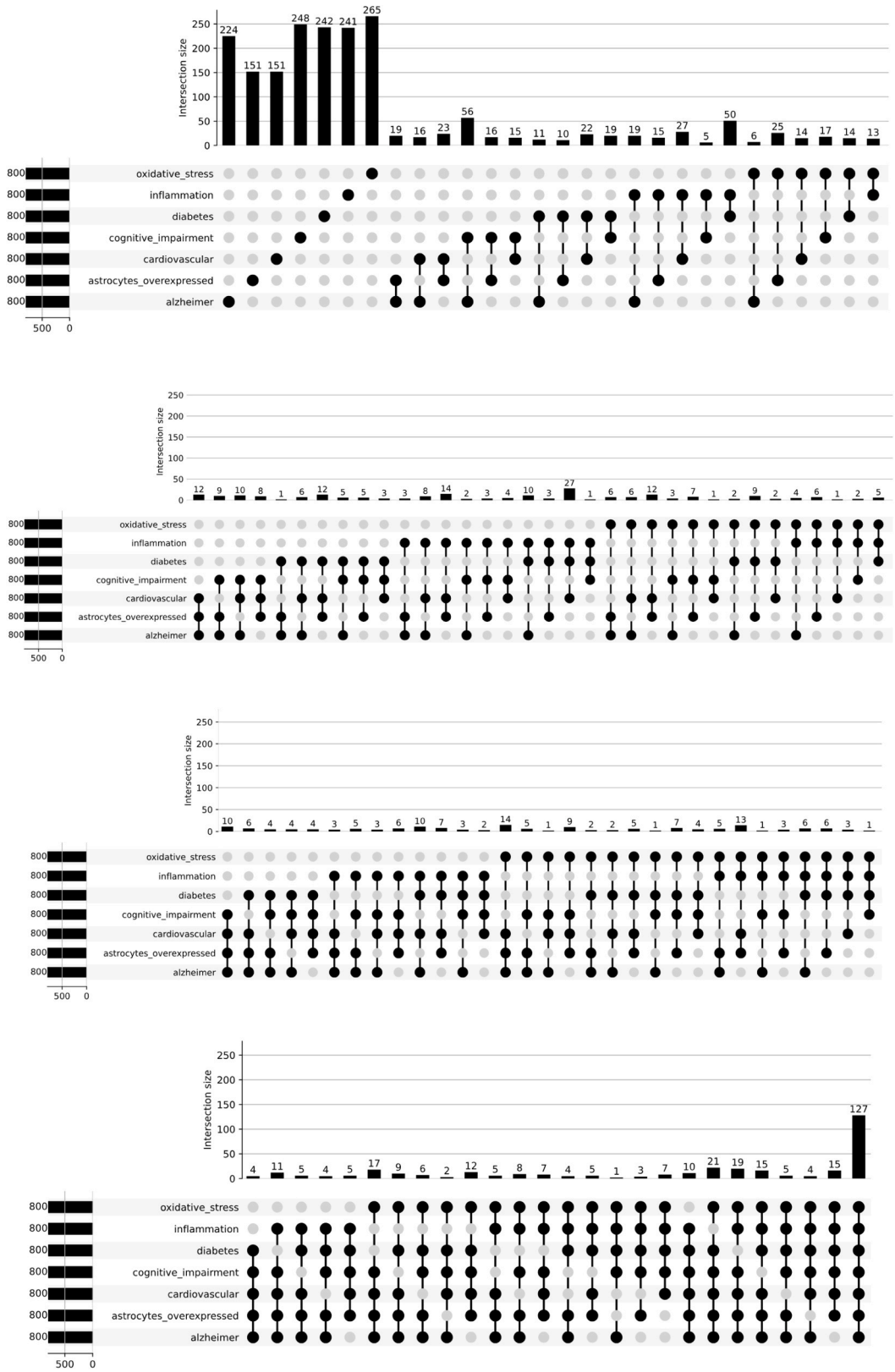



**Fig. 2.** UpSet Plot of Shared Genes Across Phenotype Networks. The plot shows intersections among the top 5 % of prioritized genes across seven networks: Alzheimer's disease (AD), cardiovascular disease (CVD), type 2 diabetes (T2D), oxidative stress (OS), inflammation (I), cognitive impairment (CI), and the astrocyte-overexpressed network (AO). Each row on the left represents one phenotype-specific gene list. Filled dots and connecting lines in the matrix indicate shared gene sets, while vertical bars above quantify the size of each intersection. The largest bar corresponds to the 127 genes present in all seven networks, defining a core molecular signature across aging-related conditions.

Downloaded from https://spj.science.org at Koc Universitesi Suna Kirac on July 02, 2026

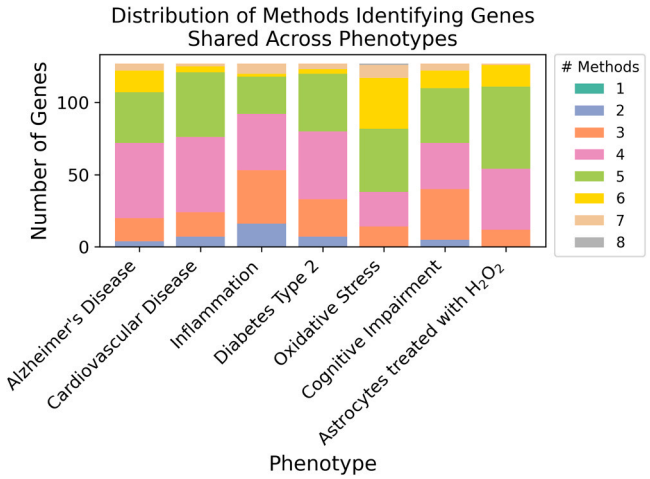



**Fig. 3.** Stacked Bar Chart of Method Consensus per Phenotype. For each of the seven phenotypes (AD, CVD, T2D, OS, I, CI, AO), the stacked bar indicates how many of the eight topology-based ranking methods in GUILD identified each gene within the top 5 % of prioritized candidates. The x-axis shows phenotypes, and the y-axis indicates the number of top-ranked genes. Colored segments represent the number of methods supporting each gene-disease predicted association (from 1 to 8). Higher segments reflect stronger consensus, with the top segments representing genes recognized by all eight methods. This visualization highlights the robustness of gene prioritization across analytic approaches.

with potential loss-of-interaction mechanisms in these modeled complexes (Table 2). A representative example is the nuclear lamin heterodimer (LMNA–LMNB1), where multiple lamin-A missense variants associated with laminopathies cluster at the interface. LMNA I373F and I373S showed among the largest ΔΔG increases (> +2.3 kcal/mol), consistent with a substantial weakening of the modeled heterodimer interface; additional interface variants (R377H, L380S) also yielded positive ΔΔG (+0.5–1.1 kcal/mol). Not all substitutions were destabilizing: LMNA E358K slightly decreased ΔΔG (≈ −0.4 kcal/mol), compatible with a modest stabilization of the modeled contact, which could in principle influence lamina mechanics, although this will require experimental confirmation. Together, these results are consistent with the possibility that both loss and gain of binding at A–B lamin contacts can perturb nuclear mechanics, chromatin tethering, and stress responses linked to aging phenotypes [103,104]. A second prominent module involves the actin cytoskeleton, particularly α-actinin-4 (ACTN4) complexes with filamins (FLNB and FLNC). Variants originally linked to kidney disease or myopathy often fell directly at the ACTN4–filamin interface105, [106]. For example, ACTN4 K255E, a familial FSGS mutation [107], was predicted to weaken binding (ΔΔG ≈ +0.8 to +1.1 kcal/mol across ACTN4–FLNB/FLNC), potentially compromising actin crosslinking and mechanotransduction [108]. Notably, the impact of ACTN4 L169R depended on partner: it strengthened ACTN4–FLNB (ΔΔG ≈ −1.7 kcal/mol) but destabilized ACTN4–FLNC (ΔΔG ≈ +1.8 kcal/mol), illustrating context-specific effects in our modeled complexes. Conversely, ACTN4 T259I strongly stabilized ACTN4–FLNC (ΔΔG ≈ −2.4 kcal/mol), suggesting that this variant could favor tighter binding at this interface.

We also observed interface-sensitive effects on 14–3–3 dimerization [109]. In models of YWHAG/YWHAZ dimers, a L177F/L178F-like substitution yielded a moderate ΔΔG increase (≈ +1.4 kcal/mol), consistent with weakened dimer formation [110,111] and potentially reduced availability of 14–3–3 scaffolds for phospho-client signaling complexes; by contrast, YWHAZ V180A produced only a mild effect (+0.3–0.6 kcal/mol). Given the centrality of 14–3–3 in stress signaling, even modest dimer weakening could reverberate across apoptotic and metabolic pathways [112].

Finally, within the multi-aminoacyl tRNA synthetase complex (MSC), a pathogenic QARS1 R515W variant mapped directly to the QARS1–EPRS1 interface and produced one of the largest ΔΔG values we observed (≈ +5.8 kcal/mol), consistent with a destabilization of the modeled interface [113]. Dissociation of MSC components, specifically EPRS1, drives the interferon-γ/TLR-responsive GAIT pathway, which represses translation of inflammation-related

**Table 1**
Reactome Pathway Enrichment Across Astrocyte and Disease Networks. This table lists Reactome pathways that are significantly enriched (FDR-adjusted P < 0.05) in the top 5 % GUILD-prioritized genes for each of the seven networks (astrocyte-overexpressed PAOSA, AD, CVD, T2D, oxidative stress, inflammation, cognitive impairment). Only pathways that are significant in all seven subnetworks are shown, i.e. the cross-phenotype Reactome core.

| Term name | Alzheimer's DIsease | Cardiovascula r Disease | Type 2 Diabetes | Oxidative stress | Inflammation | Cognitive Impairment | Astrocytes over | Astrocytes under |
|---|---|---|---|---|---|---|---|---|
| *Selenoamino acid metabolism* | 2.84E-07 | 6.20E-08 | 2.21E-06 | 5.58E-09 | 2.84E-04 | 8.35E-04 | 2.41E-07 | |
| *Transcriptional and post-translational regulation of MITF-M expression and activity* | 5.93E-05 | 6.53E-08 | 2.98E-08 | 1.88E-06 | 3.94E-05 | 9.59E-03 | 4.38E-03 | 2.11E-02 |
| *Cytosolic tRNA aminoacylation* | 1.22E-04 | 1.45E-06 | 2.65E-03 | 2.23E-08 | 2.55E-02 | 1.26E-02 | 3.94E-09 | |
| *HSF1 activation* | 2.00E-04 | 7.40E-05 | 1.97E-03 | 7.60E-03 | 1.48E-03 | 4.37E-04 | 4.60E-05 | 1.43E-02 |
| *SARS-CoV-1 targets host intracellular signalling and regulatory pathways* | 4.85E-04 | 6.20E-08 | 4.01E-04 | 1.37E-04 | 2.38E-05 | 6.62E-05 | 1.56E-03 | 4.03E-03 |
| *Signaling by phosphorylated juxtamembrane, extracellular and kinase domain KIT mutants* | 5.40E-04 | 4.66E-03 | 4.11E-02 | 2.89E-02 | 3.08E-02 | 4.34E-03 | 1.19E-03 | 4.61E-02 |
| *SARS-CoV-2 targets host intracellular signalling and regulatory pathways* | 1.07E-03 | 3.80E-04 | 9.40E-05 | 4.03E-04 | 6.01E-03 | 1.95E-03 | 4.68E-03 | 1.02E-03 |
| *Initiation of Nuclear Envelope (NE) Reformation* | 2.38E-03 | 3.27E-05 | 1.13E-02 | 1.60E-05 | 7.81E-03 | 2.20E-05 | 1.19E-03 | 4.61E-02 |
| *Signaling by RAS GAP mutants* | 1.01E-02 | 4.55E-03 | 1.13E-02 | 6.56E-03 | 7.52E-03 | 1.26E-02 | 6.43E-03 | 1.28E-02 |
| *Regulation of HSF1-mediated heat shock response* | 1.65E-02 | 5.20E-05 | 2.76E-03 | 1.26E-06 | 1.27E-02 | 8.35E-04 | 4.22E-04 | 3.53E-03 |
| *Activation of BAD and translocation to mitochondria* | 1.71E-02 | 8.08E-03 | 4.01E-04 | 1.63E-03 | 2.47E-03 | 2.05E-02 | | 2.11E-02 |
| *CD209 (DC-SIGN) signaling* | 1.71E-02 | 1.93E-03 | 4.78E-03 | 4.55E-02 | 3.68E-03 | 2.04E-02 | | 2.11E-02 |
| *EGFR Transactivation by Gastrin* | 2.80E-02 | 1.45E-02 | 4.78E-03 | 1.55E-04 | 3.59E-03 | 6.61E-03 | | 6.12E-03 |
| *Calnexin/calreticulin cycle* | 4.49E-02 | 2.12E-03 | 4.98E-02 | 2.97E-03 | 3.59E-02 | 4.18E-02 | 3.63E-02 | |
| *Activation of RAS in B cells* | 4.49E-02 | 2.52E-02 | 4.98E-02 | 3.65E-02 | 3.59E-02 | 4.18E-02 | 3.63E-02 | |

Downloaded from https://spj.science.org at Koc Universitesi Suna Kirac on July 02, 2026

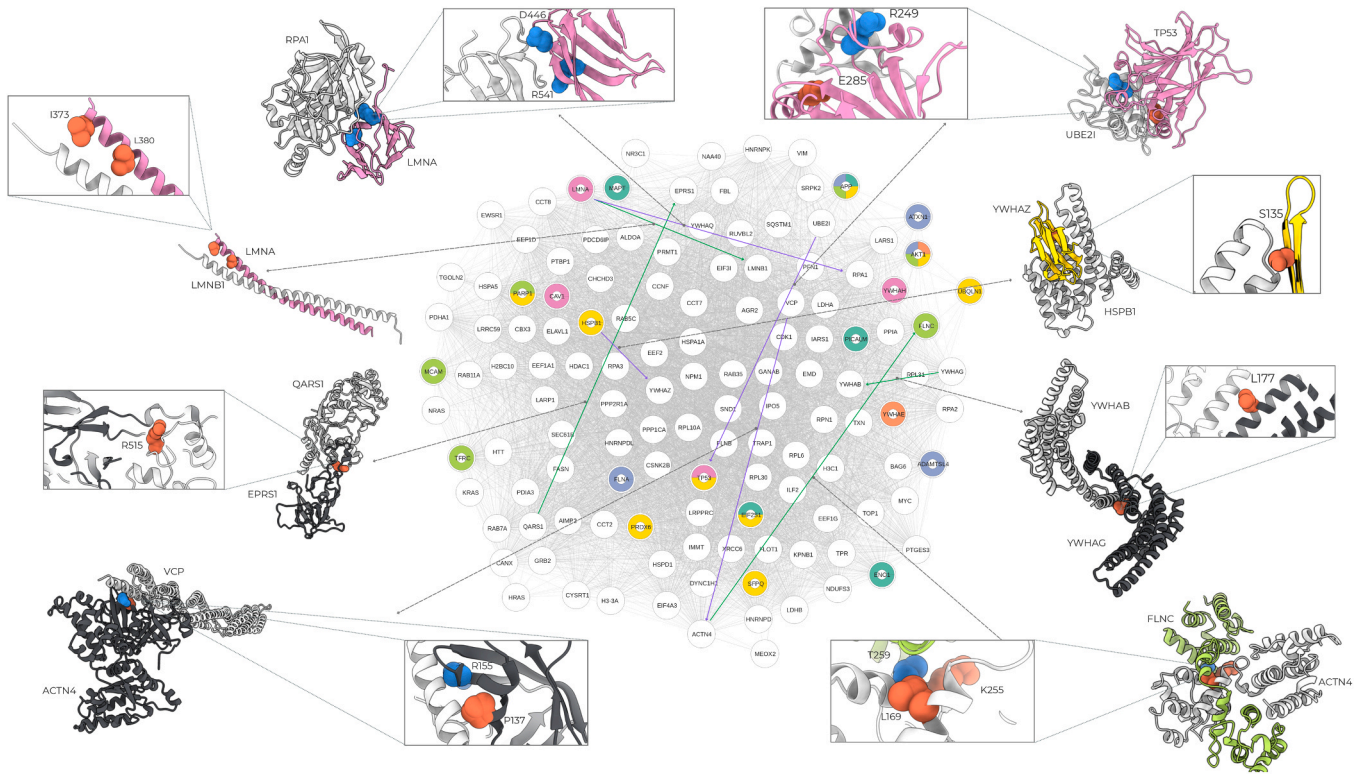



**Fig. 4.** Cross-phenotype 127-gene interactome with CM2D3 structural support and variant effects. Cytoscape network of the 127 genes shared across astrocyte oxidative stress and six aging-related pathophenotypes. Node colors mark seed membership to each pathophenotype (see legend below); white nodes are non-seed genes within the shared core. Multi-phenotype seeds are rendered as pie-chart nodes with segment colors indicating phenotype memberships. Edges denote PPIs with structural models from CM2D3 (green for homology/template-based complexes and violet for docking-derived complexes). Structural insets (rendered in Chimera) show representative interfaces; zoomed residues indicate missense positions whose mutations alter binding energies computed with FoldX (ΔΔG_interface = mutant − wild-type). Residues depicted with atom-spheres in red indicate destabilizing mutations and hyperstabilizing mutations are shown in blue. Phenotype color legend: Diabetes (Pink), Cardiovascular (Orange), Inflammation (Green), Alzheimer (Turquoise), Oxidative Stress (Yellow), and Cognitive Impairment (Blue).

**Table 2**
Structural perturbations at PPI interfaces in comparative (homology-based) models. Summary of key pathogenic missense variants mapped onto interfaces of 3D complexes obtained via CM2D3 template-based modeling. For each mutated protein and its binding partner, the specific amino-acid substitution is listed along with the FoldX-calculated change in binding free energy (ΔΔG = mutant – wild-type) in kcal/mol. Positive ΔΔG values indicate destabilizing mutations (loss of interaction affinity), whereas negative values indicate stabilizing (gain-of-binding) effects.

| Mutated protein | Partner protein | Mutation | ΔΔG |
|---|---|---|---|
| YWAHG (14–3–3 protein gamma) 1433G_HUMAN | YWHAB (14–3–3 protein beta/alpha) 1433B_HUMAN | L177F | 1.462 |
| ACTN4 (Alpha-actinin-4) ACTN4_HUMAN | FLNB (Filamin-B) FLNB_HUMAN | L169R | -1.703 |
| ACTN4 (Alpha-actinin-4) ACTN4_HUMAN | FLNC (Filamin-C) FLNC_HUMAN | L169R | 1.843 |
| ACTN4 (Alpha-actinin-4) ACTN4_HUMAN | FLNC (Filamin-C) FLNC_HUMAN | T259I | -2.423 |
| ACTN4 (Alpha-actinin-4) ACTN4_HUMAN | FLNC (Filamin-C) FLNC_HUMAN | K255E | 1.060 |
| FLNC (Filamin-C) FLNC_HUMAN | FLNB (Filamin-B) FLNB_HUMAN | M251T | -2.111 |
| LMNA (Prelamin-A/C) LMNA_HUMAN | LMNB1 (Lamin-B1) LMNB1_HUMAN | I373F | 2.987 |
| LMNA (Prelamin-A/C) LMNA_HUMAN | LMNB1 (Lamin-B1) LMNA_HUMAN | I373S | 2.379 |
| LMNA (Prelamin-A/C) LMNA_HUMAN | LMNB1 (Lamin-B1) LMNA_HUMAN | L380S | 1.106 |
| QARS1 (Glutamine–tRNA ligase) SYQ_HUMAN | EPRS1 (Glutamyl-prolyl-tRNA synthetase) SYEP_HUMAN | R515W | 5.811 |

mRNAs [114,115]. Variants that markedly affect this contact could, in principle, modulate proteostasis pressure and chronic inflammation. Docking-based complexes revealed diverse, partner-specific effects (Table 3). In LMNA–RPA1, LMNA D446N and R541G returned very large negative ΔΔG values (≈ −18.7 and −10.2 kcal/mol), indicating a more favorable binding in this docking-derived model and pointing to LMNA–RPA1 as a potentially sensitive contact for nuclear stability in aging-associated disease phenotypes. By comparison, LMNA variants in complexes with EEF1D and TPR had more moderate predicted effects. However, ΔΔG values exceeding ±5 kcal/mol derived from docking-based models should be interpreted with caution, as such large changes may reflect uncertainties or structural imprecision inherent to docking-generated complexes rather than true energetic effects of the variants.

For TP53–UBE2I (UBC9), we observed both directions of change: TP53 R249S showed a negative ΔΔG (≈ −3.4 kcal/mol), compatible with stronger association in our model and potentially altered SUMOylation dynamics, whereas TP53 E285K showed a positive ΔΔG (≈ +2.3 kcal/mol), compatible with a weakening of the modeled complex. The VCP (p97; formerly TERA)–ACTN4 interface was especially sensitive in our docking-derived models: VCP R155G yielded a very large negative ΔΔG (≈ −23.8 kcal/mol), while nearby P137L gave a large positive value (≈ +5.5 kcal/mol), indicating that small sequence changes at this site can strongly shift the predicted interaction. Stress-response chaperone interfaces were similarly variant-sensitive: HSPB1 S135Y was associated with a large positive ΔΔG for HSPB1–14–3–3ζ (≈ +9.6 kcal/mol), consistent with a strong weakening of this modeled interaction, whereas R140G gave a

Downloaded from https://spj.science.org at Koc Universitesi Suna Kirac on July 02, 2026

**Table 3**
Structural perturbations at PPI interfaces in docking-derived models. Summary of key pathogenic missense variants mapped onto interfaces of complexes generated by ab initio docking. Each row gives the mutated protein and its docking partner, the residue change, and the FoldX ΔΔG (kcal/mol). As before, positive ΔΔG denotes predicted weakening of the interaction, and negative ΔΔG denotes predicted strengthening.

| Mutated protein | Partner protein | Mutation | ΔΔG (kcal/mol) |
|---|---|---|---|
| LMNA (Prelamin-A/C) LMNA_HUMAN | RPA1 (Replication protein A 70 kDa DNA-binding subunit) RFA1_HUMAN | D446N | -18.738 |
| LMNA (Prelamin-A/C) LMNA_HUMAN | RPA1 (Replication protein A 70 kDa DNA-binding subunit) RFA1_HUMAN | R541G | -10.219 |
| TP53 (Cellular tumor antigen p53) P53_HUMAN | UBE2I (SUMO-conjugating enzyme UBC9) UBC9_HUMAN | R249S | -3.444 |
| TP53 (Cellular tumor antigen p53) P53_HUMAN | UBE2I (SUMO-conjugating enzyme UBC9) UBC9_HUMAN | E285K | 2.337 |
| VCP (Transitional endoplasmic reticulum ATPase) TERA_HUMAN | ACTN4 (Alpha-actinin-4) ACTN4_HUMAN | R155G | -23.848 |
| VCP (Transitional endoplasmic reticulum ATPase) TERA_HUMAN | ACTN4 (Alpha-actinin-4) ACTN4_HUMAN | P137L | 5.457 |
| HSPB1 (Heat shock protein beta-1) HSPB1_HUMAN | YWHAZ (14–3–3 protein zeta/delta) 1433Z_HUMAN | S135Y | 9.585 |
| HSPB1 (Heat shock protein beta-1) HSPB1_HUMAN | ACTN4 (Alpha-actinin-4) 1433Z_HUMAN | R140G | -3.385 |

more moderate negative ΔΔG for HSPB1–14–3–3β (≈ −3.4 kcal/mol), compatible with stabilization.

In parallel, we leveraged PRISM to obtain interface predictions for selected high-priority interactions among the top-ranked overlap genes, focusing on pairs not structurally covered by CM2D3. PRISM identifies candidate complexes by matching surface patches of the target proteins to complementary sides of experimentally resolved template interfaces and ranks them by a global interaction-energy score, with more negative values indicating more favorable interfaces. We interpreted these PRISM-derived complexes alongside the CM2D3/FoldX ΔΔG_interface results as orthogonal structural hypotheses for specific subnetworks. Within this subset, two motifs were particularly prominent: (i) a 14–3–3 signaling hub, in which YWHAZ engages TP53, AKT1, VIM, and STK11-containing assemblies, and (ii) an amyloid precursor protein (APP)–proteostasis axis connecting APP and γ-secretase conformers to valosin-containing protein (VCP/p97). The full set of PRISM predictions, together with the CM2D3 models and ClinVar-mapped mutations, is available in the GitHub repository (see Data & Code Availability).

## 5. Discussion

This work links a human astrocyte OS model to disease mechanisms by integrating transcriptomics, network-based prioritization, and structure-guided variant interpretation. Three main conclusions emerge. First, sublethal OS rewires astrocytes toward a state that simultaneously boosts proteostasis safeguards and translational control while inhibiting chromatin/transcriptional programs, an adaptive but potentially brittle configuration if stress persists. Furthermore, the comparison between this induced oxidative stress to a previously published astrocyte senescence signature [117] revealed a significant overlap (30 out of 81 genes, with a p-value $2.5 \times 10^{-4}$), indicating that oxidative stress triggers transcriptional programs partially convergent with ageing- and senescence-associated remodeling in astrocytes (see details in "Data and Code availability" section).

Second, when embedded in the human interactome and projected onto aging-associated phenotypes (AD, CVD, T2D, CI, inflammation, OS), these astrocytic signals converge on a shared 127-gene core enriched for proteostasis, DNA repair, mitochondrial regulation, and telomere/nuclear-envelope maintenance. Third, structural modeling, combining CM2D3 complexes with PRISM-derived complexes for high-priority pairs lacking templates, pinpoints variants that may perturb these systems and highlights structurally plausible interfaces, outlining potential mechanistic routes from network hubs to cellular failure modes.

The phenotype-stratified subnetworks capture canonical disease axes but also reveal their overlap within astrocytes. AD- and CI-focused analyses highlight ER-associated folding/clearance, insulin/IGF signaling, synaptic support, and nitric-oxide/cerebrovascular coupling features that are also represented in the CVD network via endothelial function, lipid handling, and circadian regulation. The T2D subnetwork reinforces immunometabolic crosstalk (INSR/IRS/AKT pathways with NF-κB and oxidative defenses), while the inflammation and OS networks embed these same regulators in stress-adaptation circuits. The 127-gene intersection highlights a shared prioritized module in our interactome analyses, consistent with the hypothesis that common stress-response programs are repeatedly implicated across these phenotypes. Notably, recurring non-seed hubs, TGOLN2 (secretory sorting), the RPA1–3 complex (replication/repair), and LMNA (nuclear lamina), bridge modules that are often treated separately (secretory traffic, genome maintenance, and mechanotransduction), providing a plausible mechanistic framework that could help explain the observed comorbidity, without establishing causality. A salient theme is envelope/genome stability: enrichment for positive regulation of telomere maintenance and initiation of nuclear-envelope reformation dovetails with the prominence of LMNA and replication-stress nodes (RPA, ATR/ERCC factors). In parallel, proteostasis emerges as a central pillar (HSF1 activation, calnexin/calreticulin cycle, cytosolic tRNA aminoacylation), consistent with the transcriptional up-shift of chaperone and translational quality-control genes. Together, these results motivate a model in which persistent oxidative stress may reprogram astrocyte signaling and trafficking in ways that could contribute to neurovascular and systemic dysfunction. Mapping ClinVar missense variants onto CM2D3 complexes showed that many disease-linked substitutions likely weaken PPIs (positive ΔΔG), but “gain of binding” also appears pathogenic in specific contexts. Because ClinVar variants are already annotated as disease-associated, our variant/interface and ΔΔG analyses are used only to propose mechanistic hypotheses for prioritized interactions and are not treated as independent validation of the network–phenotype links. The LMNA–LMNB1 heterodimer illustrates both behaviors: several lamin-A variants markedly destabilize the interface, while others modestly stabilize it, implying that either lamina fragility or pathological stiffening could impair mechanotransduction, DNA-damage responses, and stress resilience. In the actin–adhesion module, ACTN4 substitutions exert partner-specific effects on filamin binding, consistent with altered crosslinking and force transmission processes relevant to astrocyte morphology, perivascular endfoot integrity, and BBB support. For 14–3–3 scaffolds, dimer-weakening substitutions may reduce the availability of client-binding platforms that coordinate phosphosignaling under stress, with ramifications for apoptosis and metabolic control. Within the multi-aminoacyl-tRNA synthetase complex, the large ΔΔG predicted for QARS1–EPRS1 disruption points to a potential route by which interface perturbations could challenge proteostasis and favor aberrant inflammatory translation (GAIT), offering a plausible connection between redox stress and chronic inflammation.

PRISM analyses supplied orthogonal structural support in the subset of high-priority interactions lacking CM2D3 complexes. Several hubs repeatedly achieved favorable interface matches with strongly negative global energies, including: (i) a 14–3–3 (YWHAZ/YWHAG) hub engaging TP53, AKT1, VIM, and STK11-containing assemblies; (ii) an

Downloaded from https://spj.science.org at Koc Universitesi Suna Kirac on July 02, 2026

APP–proteostasis axis connecting APP/γ-secretase conformers to VCP/p97. These predicted complexes suggest potential links between proteostasis and APP handling (APP–VCP) and between checkpoint/survival signaling and 14–3–3 scaffolding, generating testable hypotheses for follow-up. The cross-phenotype core suggests that biomarkers and interventions targeting common nodes may yield benefits across neurodegenerative and cardiometabolic spectra. We nominate secretory-pathway components (e.g., TGOLN2-linked cargo/trafficking readouts), lamina-derived signatures, and DNA-damage/repair markers (RPA-associated) as biomarker candidates for evaluation in future patient-relevant studies. Therapeutically, three leverage points emerge: (1) proteostasis reinforcement (HSF1/UPR tuning, selective autophagy/ERAD enhancement); (2) nuclear-envelope/genome-stability support (modulating lamin dynamics, DDR signaling, oxidative DNA-repair capacity); and (3) scaffolded signaling control (stabilizing 14–3–3 dimer/client interactions or correcting hyper-stabilized/unstable variant interfaces). The APP–VCP hypothesis motivates testing whether p97 modulation or trafficking/chaperone perturbations affect APP/γ-secretase routing in astrocytes, with dual readouts in amyloid processing and vascular/endothelial crosstalk.

From a structural perspective, all CM2D3 and PRISM complexes analyzed here are predicted rather than experimentally resolved, and the associated FoldX ΔΔG values are typically accurate to within approximately 1–2 kcal/mol on curated benchmarks, with larger deviations expected for individual cases and especially for docking-only models. We therefore treat both the modeled interfaces and the corresponding ΔΔG shifts as qualitative, model-dependent hypotheses about sensitive protein–protein contacts, and we focus on the direction and relative magnitude of predicted effects rather than on their absolute energetic values.

We must note that the cellular experimental methodology employed presents certain limitations. Firstly, the induction of OS using a sublethal $H_2O_2$ concentration represents a focused approach to modeling astrocyte changes associated with aging, which encompasses multiple biological hallmarks not covered by our model. Moreover, this acute OS models an initial damage response, rather than the full, chronic phenotype of astrocyte senescence due to persistent OS. Unlike the acute response, chronic OS involves a sustained and progressive accumulation of damage, mainly characterized by mitochondrial dysfunction, plasma membrane impairment, and progressive DNA damage [116]; interestingly, these events have been highlighted by our bioinformatics analysis. Secondly, the study was conducted exclusively on a single human astrocyte cell line, which warrants caution when generalizing the results to *in vivo* cellular diversity. Nevertheless, the fundamental insights derived from these detailed transcriptomic data are robust enough to pave the way for subsequent hypothesis-driven investigations across neurodegenerative and cardiovascular pathologies.

## Author statement

All authors have contributed to this work and have approved the final version of the manuscript for submission. The authors confirm that the data and code supporting the findings of this study are publicly available at the GitHub repository:https://github.com/abotlp/Astrocytes_paper

with full details provided in the Data & Code Availability section of the manuscript. The analyses, results, and interpretations reported are based on original research conducted by the authors. Artificial intelligence–based tools were used solely to assist in improving the clarity, organization, and language of the manuscript text; no AI tools were used to generate data, perform analyses, or draw scientific conclusions. The authors take full responsibility for the content of the manuscript and confirm that it accurately reflects their work.

## CRediT authorship contribution statement

**Patrick Gohl:** Writing – review & editing, Software, Methodology, Investigation. **Narcis Fernandez-Fuentes:** Writing – review & editing, Software, Methodology, Formal analysis, Conceptualization. **Baldomero Oliva:** Writing – review & editing, Supervision, Software, Resources, Methodology, Investigation, Formal analysis, Conceptualization. **Molina-Fernandez Ruben:** Writing – review & editing, Software, Methodology. **Muñoz Francisco Jose:** Writing – review & editing, Validation, Supervision, Resources, Project administration, Methodology, Investigation, Funding acquisition, Formal analysis, Data curation, Conceptualization. **Attila Gursoy:** Writing – review & editing, Supervision, Software, Resources, Project administration, Methodology, Investigation, Funding acquisition, Data curation, Conceptualization. **Oriol Bagudanch:** Writing – review & editing, Formal analysis, Data curation. **Ozlem Keskin:** Writing – review & editing, Software, Resources, Methodology, Funding acquisition, Conceptualization. **Simge Senyuz:** Writing – review & editing, Software, Methodology, Data curation. **Jordi Garcia-Ojalvo:** Writing – review & editing, Supervision, Resources, Project administration, Methodology, Funding acquisition, Conceptualization. **Zeylan Melisa E:** Writing – review & editing, Software, Methodology, Formal analysis, Data curation. **Albert Puig-Pijoan:** Writing – review & editing, Methodology, Conceptualization. **Saja Almabhouh:** Writing – review & editing, Visualization, Validation, Software, Methodology, Investigation, Formal analysis, Data curation. **Angel Ois:** Writing – review & editing, Resources, Project administration, Methodology, Funding acquisition, Conceptualization. **Hugo Fanlo-Ucar:** Writing – review & editing, Methodology, Investigation, Formal analysis. **Stanley Nattel:** Writing – review & editing, Methodology, Conceptualization. **Picon-Pages Pol:** Writing – review & editing, Validation, Methodology, Investigation, Formal analysis, Conceptualization. **Raul Vicente:** Writing – review & editing, Methodology, Conceptualization. **Bota Patricia Mirela:** Writing – review & editing, Writing – original draft, Visualization, Validation, Supervision, Software, Methodology, Investigation, Formal analysis, Data curation, Conceptualization. **Eduard Barbu:** Writing – review & editing, Software, Investigation, Conceptualization.

## Declaration of Competing Interest

I declare we have no conflict of interest.

## Acknowledgements

This work was funded by the Spanish Institute of Health Carlos III by project reference AC20/00009 -FEDER/UE and ERANET ERA-CVD_JTC2020–015. This work was also supported by the Spanish Ministry of Science and Innovation and Agencia Estatal de Investigación plus FEDER Funds through grants PID2023–150068OB-I00 funded by MICIU/AEI/10.13039/501100011033 and by 'ERDF A way of making Europe' (BO) and PID2023–149767OB-I00 funded by MICIU/AEI/10.13039/501100011033 and by 'ERDF A way of making Europe' (FJM), and, 'Unidad de Excelencia María de Maeztu' CEX2024–001431-M, funded by MICIU/AEI/10.13039/501100011033. This project was funded in part by TUBITAK Research GrantNo: 220N252 (AG). S. A. acknowledges the support provided by Erasmus+ for the study program. The authors thank the Scientific Computing Core Facility (MELIS-UPF).

## Appendix A. Supporting information

Supplementary data associated with this article can be found in the online version at doi:10.1016/j.csbj.2025.12.032.

Downloaded from https://spj.science.org at Koc Universitesi Suna Kirac on July 02, 2026

## Data availability

Data and code are publicly available at https://github.com/abotlp/Astrocytes_paper. Within the repository, all analysis outputs are organized under Astrocytes_project/GUILDifyTools-main/astrocytes. For each phenotype (alzheimer, cardiovascular, cognitive_impairment, diabetes, inflammation, oxidative_stress) and for the astrocyte runs (astrocytes_overexpressed, astrocytes_underexpressed), the seed genes are listed in seeds.txt, the consensus GUILD ranking is provided in guild_scores.txt, and functional enrichment tables (GO BP/MF and Reactome) are in "enrichment.GObp.*", "enrichment.GOmf.*", and "enrichment.Reactome.*". Cross-network overlap results are in network_overlap_over5 and network_overlap_under5, including the shared gene lists (protein_overlap_results.txt), pathway overlaps (function_overlap_results.txt), and the overlap subnetworks (subnetwork_genes.sif). For full details of the negative control analysis, including the list of unrelated phenotypes and the corresponding GUILD-based results, the reader is referred to the GitHub section in GUILDifyTools-main, "unrelated phenotypes"). All analyses are built on the BIANA-derived human protein-protein interaction network available in Astrocytes_project/BIANA_phy. The complete set of mutation analyses referenced in the paper (FoldX ΔΔG summaries and ClinVar mappings) is available under Astrocytes_project/ddg_analysis. The comparison between differentially expressed genes (DEGs) identified in human astrocytes under $H_2O_2$-induced oxidative stress and a previously published astrocyte senescence signature is shown in the GitHub section compare_Limbad.

## References


[1] Verkhratsky A, Nedergaard M. Physiology of astroglia. Physiol Rev 2018;98:239–389.
[2] Calvetti D, Somersalo E. Ménage à Trois: the role of neurotransmitters in the energy metabolism of astrocytes, glutamatergic, and GABAergic neurons. J Cereb Blood Flow Metab 2012;32:1472–83.
[3] Covelo A, Araque A. Neuronal activity determines distinct gliotransmitter release from a single astrocyte. eLife 2018;7:e32237.
[4] Falcón-Moya R, et al. Astrocyte-mediated switch in spike timing-dependent plasticity during hippocampal development. Nat Commun 2020;11:4388.
[5] Alberini CM, Cruz E, Descalzi G, Bessières B, Gao V. Astrocyte glycogen and lactate: new insights into learning and memory mechanisms. Glia 2018;66:1244–62.
[6] Tajes M, et al. The blood-brain barrier: structure, function and therapeutic approaches to cross it. Mol Membr Biol 2014;31:152–67.
[7] Fanlo-Ucar H, Picón-Pagès P, Herrera-Fernández V, ILL-Raga G, Muñoz FJ. The dual role of amyloid beta-peptide in oxidative stress and inflammation: unveiling their connections in Alzheimer's disease etiopathology. Antioxidants 2024;13:1208.
[8] Sobolczyk M, Boczek T. Astrocytic calcium and cAMP in Neurodegenerative diseases. Front Cell Neurosci 2022;16:889939.
[9] Chen Y, et al. The role of astrocytes in oxidative stress of central nervous system: a mixed blessing. Cell Prolif 2020;53:e12781.
[10] Yang T, Sun Y, Lu Z, Leak RK, Zhang F. The impact of cerebrovascular aging on vascular cognitive impairment and dementia. Ageing Res Rev 2017;34:15–29.
[11] Roger VL. Epidemiology of heart failure: a contemporary perspective. Circ Res 2021;128:1421–34.
[12] Hakim A. Ng, & Turek. Heart disease as a risk factor for dementia. Clin Epidemiol 2013;135. https://doi.org/10.2147/CLEP.S30621.
[13] Zuo W, Wu J. The interaction and pathogenesis between cognitive impairment and common cardiovascular diseases in the elderly. 20406223211063020 Ther Adv Chronic Dis 2022;13. 20406223211063020.
[14] Testai FD, et al. Cardiac contributions to brain health: a scientific statement from the american heart association. Stroke 2024;55.
[15] Lorius N, et al. Vascular disease and risk factors are associated with cognitive decline in the Alzheimer disease spectrum. Alzheimer Dis Assoc Disord 2015;29:18–25.
[16] Emrani S, et al. Alzheimer's/vascular spectrum dementia: classification in addition to diagnosis. J Alzheimer'S Dis 2020;73:63–71.
[17] Fatima G, et al. Vascular and glymphatic dysfunction as drivers of cognitive impairment in Alzheimer's disease: Insights from computational approaches. Neurobiol Dis 2025;208:106877.
[18] González-Reyes RE, Nava-Mesa MO, Vargas-Sánchez K, Ariza-Salamanca D, Mora-Muñoz L. Involvement of Astrocytes in Alzheimer's disease from a neuroinflammatory and oxidative stress perspective. Front Mol Neurosci 2017;10:427.
[19] Phatnani H, Maniatis T. Astrocytes in Neurodegenerative disease: Table 1. Cold Spring Harb Perspect Biol 2015;7:a020628.
[20] Shabir O, Berwick J, Francis SE. Neurovascular dysfunction in vascular dementia, Alzheimer's and atherosclerosis. BMC Neurosci 2018;19:62.
[21] Shen Z, Li Z-Y, Yu M-T, Tan K-L, Chen S. Metabolic perspective of astrocyte dysfunction in Alzheimer's disease and type 2 diabetes brains. Biomed Pharm 2023;158:114206.
[22] López-Otín C, Blasco MA, Partridge L, Serrano M, Kroemer G. Hallmarks of aging: An expanding universe. Cell 2023;186:243–78.
[23] Garcia-Garcia J, Guney E, Aragues R, Planas-Iglesias J, Oliva B. Biana: a software framework for compiling biological interactions and analyzing networks. BMC Bioinforma 2010;11:56.
[24] del Toro N, et al. The IntAct database: efficient access to fine-grained molecular interaction data. Nucleic Acids Res 2022;50:D648–53.
[25] Oughtred R, et al. The BioGRID database: a comprehensive biomedical resource of curated protein, genetic, and chemical interactions. Protein Sci 2021;30:187–200.
[26] Alanis-Lobato G, Andrade-Navarro MA, Schaefer MH. HIPPIE v2.0: enhancing meaningfulness and reliability of protein–protein interaction networks. Nucleic Acids Res 2017;45:D408–14.
[27] Breuer K, et al. InnateDB: systems biology of innate immunity and beyond—recent updates and continuing curation. Nucleic Acids Res 2013;41:D1228–33.
[28] UniProt Consortium The, et al. UniProt: the Universal Protein Knowledgebase in 2025. D609–D617 Nucleic Acids Res 2025;53. D609–D617.
[29] Milacic M, et al. The Reactome Pathway Knowledgebase 2024. Nucleic Acids Res 2024;52:D672–8.
[30] Schoch CL, et al. NCBI Taxonomy: a comprehensive update on curation, resources and tools. Database J Biol Databases Curation 2020 2020.
[31] Ashburner M, et al. Gene Ontology: tool for the unification of biology. Nat Genet 2000;25:25–9.
[32] 2017. The Gene Ontology Consortium. Expansion of the Gene Ontology knowledgebase and resources. Nucleic Acids Res. 45, D331–D338.
[33] Seal RL, et al. Genenames.org: the HGNC resources in 2023. Nucleic Acids Res 2023;51:D1003–9.
[34] Kamburov A, Herwig R. ConsensusPathDB 2022: molecular interactions update as a resource for network biology. D587–D595 Nucleic Acids Res 2022;50.D587–D595.
[35] Brown KR, Jurisica I. Unequal evolutionary conservation of human protein interactions in interologous networks. Genome Biol 2007;8:R95.
[36] Piñero J, et al. DisGeNET: a comprehensive platform integrating information on human disease-associated genes and variants. Nucleic Acids Res 2017;45:D833–9.
[37] Guney E, Oliva B. Exploiting protein-protein interaction networks for genome-wide disease-gene prioritization. PLoS ONE 2012;7:e43557.
[38] Amberger JS, Bocchini CA, Schiettecatte F, Scott AF, Hamosh A. OMIM.org: online mendelian inheritance in man (OMIM®), an online catalog of human genes and genetic disorders. Nucleic Acids Res 2015;43. D789–D798.
[39] White S, Smyth P. Algorithms for estimating relative importance in networks. in Proceedings of the ninth ACM SIGKDD international conference on Knowledge discovery and data mining. Washington, D.C.: ACM; 2003. p. 266–75. https://doi.org/10.1145/956750.956782.
[40] Nabieva E, Jim K, Agarwal A, Chazelle B, Singh M. Whole-proteome prediction of protein function via graph-theoretic analysis of interaction maps. Bioinformatics 2005;21.
[41] Köhler S, Bauer S, Horn D, Robinson PN. Walking the Interactome for Prioritization of Candidate Disease Genes. Am J Hum Genet 2008;82:949–58.
[42] Vanunu O, Magger O, Ruppin E, Shlomi T, Sharan R. Associating genes and protein complexes with disease via network propagation. PLoS Comput Biol 2010;6:e1000641.
[43] Ghiassian SD, Menche J, Barabási A-L. A DIseAse MOdule detection (DIAMOnD) algorithm derived from a systematic analysis of connectivity patterns of disease proteins in the human interactome. PLOS Comput Biol 2015;11:e1004120.
[44] Benjamini Y, Hochberg Y. Controlling the false discovery rate: a practical and powerful approach to multiple testing. J R Stat Soc Ser B Stat Method 1995;57:289–300.
[45] Kosoglu K, Aydin Z, Tuncbag N, Gursoy A, Keskin O. Structural coverage of the human interactome. bbad496 Brief Bioinform 2023;25. bbad496.
[46] Mirela Bota P, et al. CM2D3: Furnishing the Human Interactome with Structural Models of Protein Complexes Derived by Comparative Modeling and Docking. J Mol Biol 2023;435:168055.
[47] Baspinar A, Cukuroglu E, Nussinov R, Keskin O, Gursoy A. PRISM: a web server and repository for prediction of protein–protein interactions and modeling their 3D complexes. W285–W289 Nucleic Acids Res 2014;42. W285–W289.
[48] Delgado J, et al. FoldX force field revisited, an improved version. Bioinformatics 2025;41:btaf064.
[49] Landrum MJ, et al. ClinVar: updates to support classifications of both germline and somatic variants. Nucleic Acids Res 2025;53:D1313–21.
[50] Banmeyer I, Marchand C, Clippe A, Knoops B. Human mitochondrial peroxiredoxin 5 protects from mitochondrial DNA damages induced by hydrogen peroxide. FEBS Lett 2005;579:2327–33.
[51] Xu F, et al. ROMO1 overexpression protects the mitochondrial cysteinome from oxidations in aging. Nat Commun 2025;16:5133.
[52] Yukitake H, Takizawa M, Kimura H. Macrophage migration inhibitory factor as an emerging drug target to regulate antioxidant response element system. Oxid Med Cell Longev 2017;2017:8584930.
[53] Joshi V, et al. A decade of boon or burden: what has the CHIP ever done for cellular protein quality control mechanism implicated in neurodegeneration and aging? Front Mol Neurosci 2016;9.


Downloaded from https://spj.science.org at Koc Universitesi Suna Kirac on July 02, 2026

[54] Sahoo, B.R. *et al.* SERF2, an RNA G4 Quadruplex Binding Protein, Promotes Stress Granule Establishment. Preprint at https://doi.org/10.2139/ssrn.4836768 (2024).
[55] Zheng M, et al. Structural Features and Chaperone Activity of the NudC Protein Family. J Mol Biol 2011;409:722–41.
[56] Wang C, Tay LLE, Hu W, Corre M, Graille M. TRMT112, a master activator of several methyltransferases modifying factors involved in RNA maturation and translation. Front RNA Res 2025;3:1556979.
[57] Dewez M, et al. The conserved Wobble uridine tRNA thiolase Ctu1–Ctu2 is required to maintain genome integrity. Proc Natl Acad Sci 2008;105:5459–64.
[58] Nocella C, et al. Structure, activation, and regulation of NOX2: at the crossroad between the innate immunity and oxidative stress-mediated pathologies. Antioxidants 2023;12:429.
[59] Ribas C, et al. The G protein-coupled receptor kinase (GRK) interactome: Role of GRKs in GPCR regulation and signaling. Biochim Biophys Acta BBA Biomembr 2007;1768:913–22.
[60] Wang L, et al. Structural and functional insights into dishevelled-mediated wnt signaling. Cells 2024;13:1870.
[61] Morimoto S, et al. Rab13 Mediates the Continuous Endocytic Recycling of Occludin to the Cell Surface. J Biol Chem 2005;280:2220–8.
[62] Alterio J, et al. YIF1B Is Involved in the Anterograde Traffic Pathway and the Golgi Architecture. Traffic 2015;16:978–93.
[63] McDonald B, Schmidt MHH. Structure, function, and recombinant production of EGFL7. Biol Chem 2024;405:691–700.
[64] Lin KC, Park HW, Guan K-L. Regulation of the hippo pathway transcription factor TEAD. Trends Biochem Sci 2017;42:862–72.
[65] Kumar N, et al. VPS13A and VPS13C are lipid transport proteins differentially localized at ER contact sites. J Cell Biol 2018;217:3625–39.
[66] Boal F, Stephens DJ. Specific Functions of BIG1 and BIG2 in Endomembrane Organization. PLoS ONE 2010;5:e9898.
[67] Roberts AJ. Emerging mechanisms of dynein transport in the cytoplasm versus the cilium. Biochem Soc Trans 2018;46:967–82.
[68] Desgraupes S, Etienne L, Arhel NJ. RANBP2 evolution and human disease. FEBS Lett 2023;597:2519–33.
[69] Davis SM, Pennypacker KR. The role of the leukemia inhibitory factor receptor in neuroprotective signaling. Pharmacol Ther 2018;183:50–7.
[70] García-Navas R, et al. Critical requirement of SOS1 RAS-GEF function for mitochondrial dynamics, metabolism, and redox homeostasis. Oncogene 2021;40:4538–51.
[71] Raman M, Earnest S, Zhang K, Zhao Y, Cobb MH. TAO kinases mediate activation of p38 in response to DNA damage. EMBO J 2007;26:2005–14.
[72] Weitzman J. ATM, telomeres and aging. spotlight-20030124-01 Genome Biol 2003;4. spotlight-20030124-01.
[73] De Amicis A, et al. Role of senataxin in DNA damage and telomeric stability. DNA Repair 2011;10:199–209.
[74] Hirota S, et al. The astrocyte-expressed integrin αvβ8 governs blood vessel sprouting in the developing retina. Development 2011;138:5157–66.
[75] Islam S, Watanabe H. Versican: a dynamic regulator of the extracellular matrix. J Histochem Cytochem 2020;68:763–75.
[76] Fortugno P, et al. Recessive mutations in the neuronal isoforms of *DST*, encoding dystonin, lead to abnormal actin cytoskeleton organization and HSAN type VI. Hum Mutat 2019;40:106–14.
[77] Coquand L, et al. CAMSAPs organize an acentrosomal microtubule network from basal varicosities in radial glial cells. J Cell Biol 2021;220:e202003151.
[78] Lewerenz J, et al. The cystine/glutamate antiporter system $x_c^-$ in health and disease: from molecular mechanisms to novel therapeutic opportunities. Antioxid Redox Signal 2013;18:522–55.
[79] Bandau S, Knebel A, Gage ZO, Wood NT, Alexandru G. UBXN7 docks on neddylated cullin complexes using its UIM motif and causes HIF1α accumulation. BMC Biol 2012;10:36.
[80] Bengtson MH, Joazeiro CAP. Role of a ribosome-associated E3 ubiquitin ligase in protein quality control. Nature 2010;467:470–3.
[81] Lui TTH, et al. The ubiquitin-specific protease USP34 regulates axin stability and Wnt/β-catenin signaling. Mol Cell Biol 2011;31:2053–65.
[82] Hampel H, et al. The amyloid-β pathway in Alzheimer's disease. Mol Psychiatry 2021;26:5481–503.
[83] Zhu B, et al. ER-associated degradation regulates Alzheimer's amyloid pathology and memory function by modulating γ-secretase activity. Nat Commun 2017;8:1472.
[84] Wodrich APK, Scott AW, Shukla AK, Harris BT, Giniger E. The unfolded protein responses in health, aging, and neurodegeneration: recent advances and future considerations. Front Mol Neurosci 2022;15:831116.
[85] Lourenço CF, Laranjinha J. Nitric OXide Pathways in Neurovascular Coupling under Normal and Stress Conditions in the Brain: Strategies to Rescue Aberrant Coupling and Improve Cerebral Blood Flow. Front Physiol 2021;12:729201.
[86] Talbot K, et al. Demonstrated brain insulin resistance in Alzheimer's disease patients is associated with IGF-1 resistance, IRS-1 dysregulation, and cognitive decline. J Clin Invest 2012;122:1316–38.
[87] Boucher J, Kleinridders A, Kahn CR. Insulin receptor signaling in normal and insulin-resistant states. a009191–a009191 Cold Spring Harb Perspect Biol 2014;6. a009191–a009191.
[88] Taniguchi CM, Emanuelli B, Kahn CR. Critical nodes in signalling pathways: insights into insulin action. Nat Rev Mol Cell Biol 2006;7:85–96.
[89] Rosen ED, Spiegelman BM. What we talk about when we talk about fat. Cell 2014;156:20–44.
[90] Crnko S, Du Pré BC, Sluijter JPG, Van Laake LW. Circadian rhythms and the molecular clock in cardiovascular biology and disease. Nat Rev Cardiol 2019;16:437–47.
[91] Li J, et al. Piezo1 integration of vascular architecture with physiological force. Nature 2014;515:279–82.
[92] Kong P, et al. Inflammation and atherosclerosis: signaling pathways and therapeutic intervention. Signal Transduct Target Ther 2022;7:131.
[93] Parikh SM. Angiopoietins and Tie2 in vascular inflammation. Curr Opin Hematol 2017;24:432–8.
[94] Ridker PM, et al. Antiinflammatory therapy with canakinumab for atherosclerotic disease. N Engl J Med 2017;377:1119–31.
[95] Kawai T, Akira S. The role of pattern-recognition receptors in innate immunity: update on Toll-like receptors. Nat Immunol 2010;11:373–84.
[96] Liao JK. Linking endothelial dysfunction with endothelial cell activation. J Clin Invest 2013;123:540–1.
[97] Gao L, et al. The mechanism of linear ubiquitination in regulating cell death and correlative diseases. Cell Death Dis 2023;14:659.
[98] Jo DS, Park NY, Cho D-H. Peroxisome quality control and dysregulated lipid metabolism in neurodegenerative diseases. Exp Mol Med 2020;52:1486–95.
[99] Welch G, Tsai L. Mechanisms of DNA damage-mediated neurotoxicity in neurodegenerative disease. EMBO Rep 2022;23:e54217.
[100] Roginskaya M, Razskazovskiy Y. Oxidative DNA damage and repair: mechanisms, mutations, and relation to diseases. Antioxidants 2023;12:1623.
[101] Ge P, Dawson VL, Dawson TM. PINK1 and Parkin mitochondrial quality control: a source of regional vulnerability in Parkinson's disease. Mol Neurodegener 2020;15:20.
[102] de Magalhães JP, et al. Human ageing genomic resources: updates on key databases in ageing research. Nucleic Acids Res 2024;52:D900–8.
[103] Vahabikashi A, Adam SA, Medalia O, Goldman RD. Nuclear lamins: Structure and function in mechanobiology. APL Bioeng 2022;6:011503.
[104] Martins F, Sousa J, Pereira CD, Da Cruz E, Silva OAB, Rebelo S. Nuclear envelope dysfunction and its contribution to the aging process. Aging Cell 2020;19:e13143.
[105] Iwamoto DV, et al. Structural basis of the filamin A actin-binding domain interaction with F-actin. Nat Struct Mol Biol 2018;25:918–27.
[106] Esue O, Tseng Y, Wirtz D. α-actinin and filamin cooperatively enhance the stiffness of actin filament networks. PLoS ONE 2009;4:e4411.
[107] Kaplan JM, et al. Mutations in ACTN4, encoding α-actinin-4, cause familial focal segmental glomerulosclerosis. Nat Genet 2000;24:251–6.
[108] Ehrlicher AJ, et al. Alpha-actinin binding kinetics modulate cellular dynamics and force generation. Proc Natl Acad Sci 2015;112:6619–24.
[109] Obsil T, Obsilova V. Structural basis of 14-3-3 protein functions. Semin Cell Dev Biol 2011;22:663–72.
[110] Messaritou G, Grammenoudi S, Skoulakis EMC. Dimerization is essential for 14-3-3ζ stability and function in vivo. J Biol Chem 2010;285:1692–700.
[111] Woodcock JM, Murphy J, Stomski FC, Berndt MC, Lopez AF. The dimeric versus monomeric status of 14-3-3ζ is controlled by phosphorylation of Ser58 at the dimer interface. J Biol Chem 2003;278:36323–7.
[112] Shimada T, Fournier AE, Yamagata K. Neuroprotective function of 14-3-3 proteins in neurodegeneration. BioMed Res Int 2013;2013:1–11.
[113] Zhang X, et al. Mutations in QARS, encoding glutaminyl-tRNA synthetase, cause progressive microcephaly, cerebral-cerebellar atrophy, and intractable seizures. Am J Hum Genet 2014;94:547–58.
[114] Arif A, et al. Two-site phosphorylation of EPRS coordinates multimodal regulation of noncanonical translational control activity. Mol Cell 2009;35:164–80.
[115] Lee E-Y, et al. Glutamyl-prolyl-tRNA synthetase 1 coordinates early endosomal anti-inflammatory AKT signaling. Nat Commun 2022;13:6455.
[116] Kudryavtseva AV, et al. Mitochondrial dysfunction and oxidative stress in aging and cancer. Oncotarget 2016;7:44879–905.
[117.] Limbad C, Oron TR, Alimirah F, Davalos AR, Tracy TE, Gan L, Desprez PY, Campisi J. Astrocyte senescence promotes glutamate toxicity in cortical neurons. PLoS One 2020;15(1):e0227887.


Downloaded from https://spj.science.org at Koc Universitesi Suna Kirac on July 02, 2026

Computational and Structural Biotechnology Journal

# Oxidative stress-driven transcriptomic remodeling in human astrocytes reveals network signatures associated with neurodegenerative and cardiovascular processes

Patricia M. Bota, Pol Picón-Pagès, Hugo Fanlo-Ucar, Saja Almabhouh, Oriol Bagudanch, Melisa E. Zeylan, Simge Senyuz, Patrick Gohl, Rubén Molina-Fernández, Narcis Fernandez-Fuentes, Eduard Barbu, Raul Vicente, Stanley Nattel, Angel Ois, Albert Puig-Pijoan, Jordi Garcia-Ojalvo, Ozlem Keskin, Attila Gursoy, Francisco J. Muñoz, and Baldomero Oliva

**Citation:** Bota P, Picón-Pagès P, Fanlo-Ucar H, Almabhouh S, Bagudanch O, Zeylan M, Senyuz S, Gohl P, Molina-Fernández R, Fernandez-Fuentes N, et al. Oxidative stress-driven transcriptomic remodeling in human astrocytes reveals network signatures associated with neurodegenerative and cardiovascular processes. *Comput Struct Biotechnol J*. 2026;**31**:263-275. DOI: 10.1016/j.csbj.2025.12.032

**Abstract**

Astrocytes are central to brain homeostasis, supporting neuronal metabolism, synaptic activity, and the blood–brain barrier. With aging, these glial cells undergo molecular and functional changes that weaken support functions and promote neuroinflammation, contributing to neurodegeneration. Yet the systems-level mechanisms by which astrocytes respond to aging-related stressors remain poorly defined in human models. Because aging also heightens risk for cardiovascular disease, cognitive impairment, type 2 diabetes, and systemic inflammation, clarifying shared astrocytic pathways is critical for understanding brain–body crosstalk. Using an in vitro human astrocyte model exposed to sublethal oxidative stress (10#µM H#O#) as a proxy for age-related cellular stress, we profiled transcriptomic changes and identified differentially expressed genes across antioxidant defenses, proteostasis, transcriptional regulation, vesicular trafficking, and inflammatory signaling. We then performed network-prioritization analyses on a curated human protein–protein interactome: one seeded with the astrocyte oxidative stress responsive genes and six with phenotype-associated gene sets (Alzheimer's disease, cardiovascular disease, cognitive impairment, type 2 diabetes, oxidative stress, and inflammation). Intersecting the top 5#% scoring genes from each run yielded a 127-gene core shared across all seven, enriched for proteostasis, DNA repair, mitochondrial regulation, and telomere and nuclear envelope maintenance. Structure-guided analyses highlighted vulnerable interfaces, including lamin A/C–lamin B1, #-actinin–filamins, 14–3–3 dimers, and aminoacyl-tRNA synthetase assemblies, where pathogenic variants are predicted to destabilize or aberrantly stabilize protein interactions. Structure-based interface predictions also highlight potential interactions between amyloid precursor protein (APP) and valosin-containing protein (VCP), and between p53 and 14–3-3#, potentially linking proteostasis and stress signaling. Together, these analyses identify a conserved astrocyte-centered network signature that may relate neurodegenerative and cardiovascular processes, and prioritize structurally testable candidates for biomarker and intervention hypothesis testing.

**Graphical Abstract**

**View the article online**
https://spj.science.org/doi/10.1016/j.csbj.2025.12.032

Use of this article is subject to the Terms of service

(ISSN ) is published by the American Association for the Advancement of Science. 1200 New York Avenue NW, Washington, DC 20005.

© 2026 The Authors. Published by Elsevier B.V. on behalf of Research Network of Computational and Structural Biotechnology.

This is an open access article under the CC BY-NC-ND license (https://creativecommons.org/licenses/by-nc-nd/4.0/).

Downloaded from https://spj.science.org at Koc Universitesi Suna Kirac on July 02, 2026